YALE
PEABODY
MUSEUM

P.O. BOX 208118 | NEW HAVEN CT 06520-8118 USA | PEABODY.YALE. EDU

JOURNAL OF MARINE RESEARCH

The *Journal of Marine Research,* one of the oldest journals in American marine science, published important peer-reviewed original research on a broad array of topics in physical, biological, and chemical oceanography vital to the academic oceanographic community in the long and rich tradition of the Sears Foundation for Marine Research at Yale University.

An archive of all issues from 1937 to 2021 (Volume 1–79) are available through EliScholar, a digital platform for scholarly publishing provided by Yale University Library at https://elischolar.library.yale.edu/.

Requests for permission to clear rights for use of this content should be directed to the authors, their estates, or other representatives. The *Journal of Marine Research* has no contact information beyond the affiliations listed in the published articles. We ask that you provide attribution to the *Journal of Marine Research.*

Yale University provides access to these materials for educational and research purposes only. Copyright or other proprietary rights to content contained in this document may be held by individuals or entities other than, or in addition to, Yale University. You are solely responsible for determining the ownership of the copyright, and for obtaining permission for your intended use. Yale University makes no warranty that your distribution, reproduction, or other use of these materials will not infringe the rights of third parties.

This work is licensed under a Creative Commons Attribution-NonCommercial-ShareAlike 4.0 International License.
https://creativecommons.org/licenses/by-nc-sa/4.0/

Journal of Marine Research, 67, 119–157, 2009

Dynamics of the Indonesian seas circulation. Part I – The influence of bottom topography on temperature and salinity distributions

by Kieran T. A. O'Driscoll[1,2,3] and Vladimir M. Kamenkovich[2]

ABSTRACT

The influence of bottom topography on the distribution of temperature and salinity in the Indonesian seas region has been studied with a high-resolution model based on the Princeton Ocean Model. One of the distinctive properties of the model is an adequate reproduction of all major topographic features in the region by the model bottom relief. The three major routes of flow of Pacific water through the region have been identified. The western route follows the flow of North Pacific Water through the Sulawesi Sea, Makassar Strait, Flores Sea, and Banda Sea. This is the main branch of the Indonesian Throughflow. The eastern routes follow the flow of South Pacific water through the eastern Indonesian seas. This water enters the region either through the Halmahera Sea or by flowing to the north around Halmahera Island into the Morotai Basin and then into the Maluku Sea. A deep southward flow of South Pacific Water fills the Seram Sea below 1200 m through the Lifamatola Passage. As it enters the Seram Sea, this overflow turns eastward at depths greater than 2000 m, then upwells in the eastern part of the Seram Sea before returning westward at $\sim$1500–2000 m. The flow continues westward across the Seram Sea, spreading to greater depths before entering the Banda Sea at the Buru-Mangole passage. It is this water that shapes the temperature and salinity of the deep Banda Sea. Topographic elevations break the Indonesian seas region down into separate basins. The difference in the distributions of potential temperature, θ, and salinity, S, in adjacent basins is primarily due to specific properties of advection of θ and S across a topographic rise. By and large, the topographic rise blocks deep flow between basins whereas water shallower than the depth of the rise is free to flow between basins. To understand this process, the structure of simulated fields of temperature and salinity has been analyzed. To identify a range of advected θ or S, special sections over the sills with isotherms or isohalines and isotachs of normal velocity have been considered. Following this approach the impact of various topographic rises on the distribution of θ and S has been identified. There are no substantial structural changes of potential temperature and salinity distributions between seasons, though values of some parameters of temperature and salinity distributions, e.g., magnitudes of maxima and minima, can change. It is shown that the main structure of the observed distributions of temperature and salinity is satisfactorily reproduced by the model throughout the entire domain.

[1] U.S. Naval Oceanographic Office, Stennis Space Center, Mississippi, 39529, U.S.A.

[2] Department of Marine Science, The University of Southern Mississippi, Stennis Space Center, Mississippi, 39529, U.S.A.

[3] Present address: Institute of Oceanography, University of Hamburg, 20146 Hamburg, Germany. ***email: kieran.odriscoll@zmaw.de***

1. Introduction

The main objective of this paper is to describe the basic properties of the simulated potential temperature and salinity distributions and identify physical processes responsible for their formation. Despite numerous publications having been devoted to the circulation in the Indonesian seas, the role of South Pacific Water (SPW) and North Pacific Water (NPW) in the formation of Banda Sea water remains unclear. We present the analysis of this question. For this purpose we have developed a regional model of the Indonesian seas circulation that allowed us to calculate characteristics relevant to such an analysis (see description of the model in the Appendix). An outstanding feature of the Indonesian seas is the complexity of the bottom topography. This topography has a profound effect on the distribution of temperature and salinity in the region. In setting up the model we have taken into account all important topographic features by using high horizontal resolution and relevant smoothing of the bottom relief (see Appendix). Two water types, recognized basically by their vertical salinity structure, enter the Indonesian seas from the Pacific Ocean. NPW enters the Indonesian seas region as a branch of the Mindanao Current and is characterized by a surface salinity of ~34.10, a salinity maximum of ~34.74 at a depth of ~150 m and a deep minimum of ~34.46 at a depth of ~350–800 m. SPW enters the Indonesian seas as a branch of the New Guinea Coastal Current (NGCC) and is characterized by a surface salinity of ~34.15; a strong maximum of ~35.50 at a depth of ~100–150 m and a weak minimum of ~34.61 at a depth of ~1500 m. The temperature and salinity characteristics of NPW and SPW change as waters flow through the Indonesian seas region.

What factors control these changes? In general, the water properties are advected and diffused. We will show that below 500 m the advection is totally controlled by the blocking effect of topographic features in the region. The topographic elevations impact the advection of cold and salty water from a basin (located upstream) to the neighboring basin (located downstream). Based on CTD observations, Gordon *et al.* (2003) (see also references given therein) were able to identify the influence of the topographic feature by comparing upstream and downstream temperature and salinity distributions. But this approach on its own does not provide the whole story. It should be complemented by the analysis of distributions of normal velocities, temperature and salinity on the specially chosen sections located across the flow. Thus, using simulations of the regional model, we are able to substantially complement the traditional profile analysis.

We will identify three routes of Pacific water through the region. The first route follows the flow of NPW (the western route) through the Sulawesi Sea, Makassar Strait and Flores Sea. Along this route, the rather shallow Dewakang Sill of depth ~600 m is encountered, blocking the flow of deep saline water towards the Flores Sea and thereby towards the Banda Sea. We will show that in the upper ocean (500 m) this branch of the Indonesian Throughflow primarily consists of NPW.

The second route follows the flow of SPW (the eastern thermocline route) through the Halmahera Sea. We will show that the northern and southern Halmahera Sills completely block the flow of deep SPW into the Indonesian seas. But in the upper layer (0–500 m) some SPW can penetrate to the Maluku, Seram and Banda seas where it mixes with NPW.

The third route follows the flow of deep SPW to the north of Halmahera Island, and, after circumventing this island, through the Morotai Basin, Maluku Sea, Lifamatola Passage, Seram Sea, and into the Banda Sea (the eastern deep route). We will show that basically the salinity of the deep Banda Sea is formed due to this flow. We will discuss this view of the role of SPW in detail (see the discussion of this long standing question in e.g., Van Aken *et al.*, 1988; Godfrey *et al.,* 1993; Gordon, 1995; Godfrey and Wilkin, 1995; Gordon and Fine, 1996; Gordon *et al.*, 2003; Koch-Larrouy *et al.,* 2008; and references therein). Estimates of the simulated transports of mass, heat, and salt through the Indonesian seas region show that contributions from the deep parts of the seas to these transports are substantial (O'Driscoll, 2007). Therefore, the analysis of processes responsible for the formation of distribution of potential temperature and salinity in the deep parts of Indonesian seas (especially in the Banda Sea) is very important. We remind readers that the Banda Sea is the main source of water flowing through the Ombai Strait and Timor Passage.

In Section 2 we analyze the August simulated temperature and salinity distributions along the western route. The analysis of temperature and salinity distributions along the eastern thermocline route is presented in Section 3. In Section 4 we discuss the circulation in the Seram Sea. The analysis of temperature and salinity distributions along the eastern deep route is presented in Section 5. Seasonal variability is discussed in Section 6. Comparison with observations is discussed in Section 7. We present conclusions in Section 8.

2. The analysis of temperature and salinity distributions along the western route

The western route begins at the MC port (see Fig. A.1, Appendix, for a map of the model domain with names including open ports, seas and topographic features), through which NPW enters the region before splitting into two branches. The first branch of NPW takes the westernmost route through the Indonesian seas, flowing over the Karakelong and Sangihe ridges, across the Sulawesi Sea, and along the Makassar Strait before diverging in the south of the strait. Part of the flow exits the region through the Lombok Strait, but the main portion flows through the Flores Sea to the Banda Sea (see route $AGHIJKF$ in Fig. 1). The second branch of NPW leaves the region through the NECC port.

The main impact of bottom topography is manifested in the deep layers (greater than 500 m depth), though some influence can be also traced in the upper 500 m. Here, we analyze the August simulated data.

Consider first the transformation of temperature profiles between points $AGHIJK$ and F (Fig. 2a). In the upper 50 m profiles A, G, and H are warmer than the other profiles (by $\sim 2°\text{C}$) due to their geographic location. Then, in the layer of strong thermocline (50–300 m), and even deeper (down to 500 m), all profiles are similar. Noticeable differences appear at $\sim$ 1000 m. For depths greater than 1000 m, profile G has substantially higher temperature than initial profile A. Profiles G, H, and I practically coincide. Profile J (Flores Sea) diverges from I, becoming slightly colder below 700 m and 0.5°C colder at 1500 m.

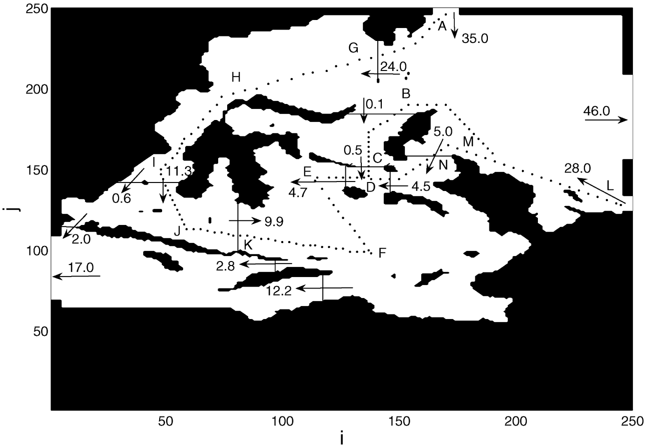

Figure 1. The locations of vertical sections $AGHIJKF$, $LMND$ and $MBCDEF$ are shown by dots. Vertical profiles of temperature and salinity are provided at points identified by letters $A, \ldots, N$. Numbers give August transports through sections shown by thin lines in Sverdrups (10^6 m^3/s) in the direction of arrows. All arrows show transport directed normally to sections; slanting of some arrows is made for convenience of plotting. Values of indices i and j are given on the x- and y-axes. The open ports are located where transports enter and leave the model domain. See Figure A.1 for model orientation and geographical names and location.

Below 1500 m, profile K (west Banda Sea) begins to diverge from profile J, but profiles K and F (both in the Banda Sea) coincide. Notice that bottom water in the Banda Sea is substantially colder than that in the Flores Sea (compare profiles K and F with profile J). The above mentioned features are also seen in the vertical section of temperature below 300 m taken along $AGHIJKF$ (Fig. 2b).

Examine the divergence of profiles A and G below 1000 m. Note that the section $AGHIJKF$ goes through a passage in the northern Sangihe Ridge with a sill at $\sim$1200 m depth (Fig. 2b). Water above sill depth is free to move across the sill, and since the deep Sulawesi Sea is warmer than the deep Pacific we suggest that the deep Sulawesi Sea basin is filled by the overflow across the sill. Isotherms $\theta < 5°\text{C}$ are blocked by the ridge while isotherms $\theta > 5°\text{C}$ pass over it. Thus, a quite different θ stratification is shaped downstream of the ridge relative to upstream.

What characteristics of the upstream flow and underwater topography determine the stratification over the Sangihe sill? This is a challenging question but we will not attempt to answer it now. We will simply demonstrate different types of overflows in the Indonesian seas region and provide some estimate of advection (of, say, salinity) into the downstream basin considered.

Below the depth of the Dewakang Sill, the Flores Sea is slightly colder than the Sulawesi Sea at any given depth, e.g., the 6°C isotherm is located at $\sim$1500 m in the Flores Sea but at $\sim$1700 m in the Makassar Strait and Sulawesi Sea. Based on the figure for θ (not given)

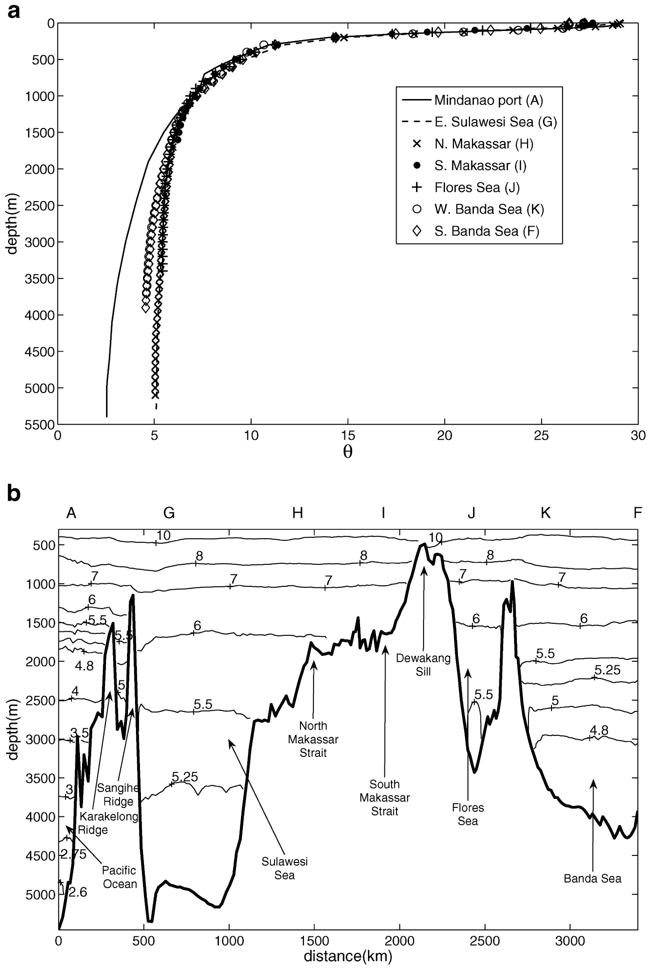

Figure 2. (a) Vertical profiles of potential temperature along the western route for August at points A, G, H, I, J, K, and F. Locations of profiles are indicated in Figure 1 and at the top of Figure 2b. (b) The distribution of potential temperature on vertical section $AGHIJKF$ below 300 m (see Fig. 1). The bottom topography along this section is shown. Locations of points A, G, H, I, J, K, and F are indicated along the top of the figure. Distance from point A is shown on the x-axis. Geographical names and locations are shown (see also Fig. A.1).

similar to Figure 5 for S we conclude that the Dewakang Sill blocks isotherms $\theta < 8°C$ from entering the Flores Sea. So where does deep Flores Sea water come from? The 6°C isotherm is located at the same depth in the Flores and west Banda seas but the Flores basin is warmer than the west Banda Sea below ~2000 m, for example the 5.5°C isotherm is situated at ~2000 m depth in the west Banda Sea and at ~2500 m in the Flores Sea, suggesting that the deep Flores basin is filled across the ridge between the Flores and Banda seas (the

Flores-Banda Ridge) with a depth of roughly 2000 m. This also explains the departure of profile *J* from *K* below 1500 m and, most importantly, leads to the conclusion that deep Banda Sea water cannot be formed along the western route (from Makassar) but must be supplied from elsewhere.

We now turn to the analysis of salinity profiles (Fig. 3a). Because these profiles contain more structure than their temperature counterparts, they will provide us with some additional

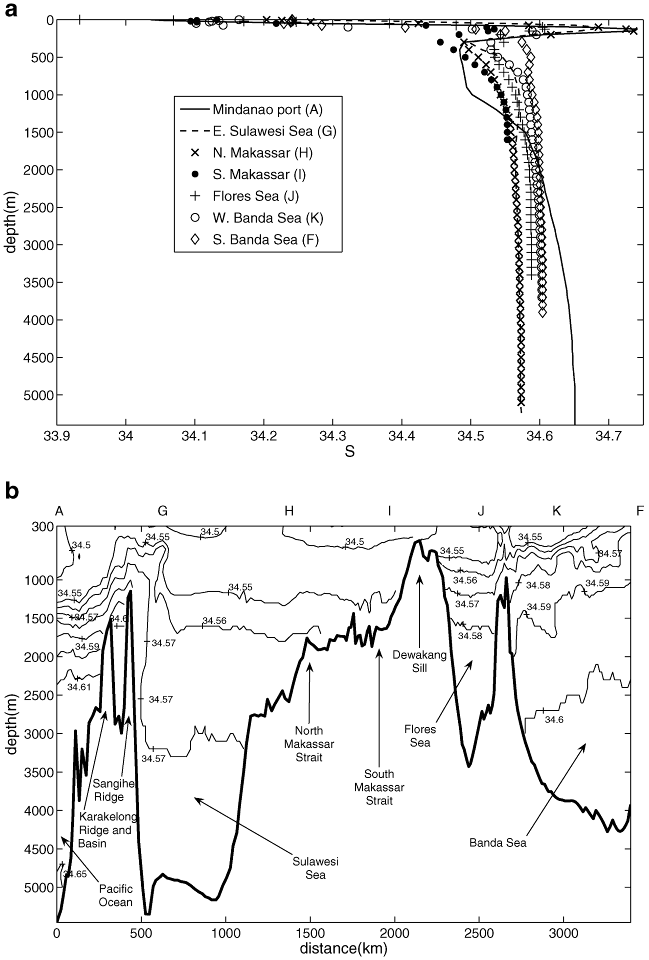

Figure 3. (a) Vertical profiles of salinity along the western route for August at points *A*, *G*, *H*, *I*, *J*, *K*, and *F*. Locations of profiles are indicated in Figure 1 and at the top of Figure 3b. (b) The distribution of salinity on vertical section *AGHIJKF* below 300 m (see Fig. 1). The bottom topography along this section is shown. Locations of points *A*, *G*, *H*, *I*, *J*, *K*, and *F* are indicated along the top of the figure. Distance from point *A* is shown on the x-axis. Geographical names and locations are shown (see also Fig. A.1).

information about the dynamics. The distinguishing feature of profile A, characteristic of NPW, is the presence of a maximum (34.74) at a depth of ~125–150 m, a minimum (34.48) at a depth of ~400 m with a slight increase to 34.49 at 800 m that is the signature of North Pacific Intermediate Water (NPIW). The structure of profiles G, H, I, J, and K in the upper ocean is basically the same; they have maxima and minima at approximately the same depths. However, the magnitudes of these extrema differ substantially; the magnitudes of the maxima generally decrease along the western route (when one moves from profile A to K), while the magnitudes of the minima generally increase. Profile F essentially has no extrema. We suggest that the process of decreasing salinity maxima and increasing of salinity minima along the western route is due to the effect of vertical diffusion, see O'Driscoll (2007) for further discussion. A more detailed picture is given by the vertical section of salinity below 300 m along $AGHIJKF$ (Fig. 3b).

We analyze now in detail salinity profiles G, H, I, J, K, and F below 500 m. First, profiles G, H, I, J, K, and F are saltier than A in the depth range 500–1300 m. Then we observe that profile G becomes less salty than A below 1400 m. This is also clearly seen in Figure 3b. There is no doubt that the deviation is caused by the blocking effect of the Sangihe Ridge, although such a separation begins at a deeper level than for temperature profiles.

The role of topographic dividers in shaping distinct stratifications in different basins can be clarified by considering the distribution of normal velocity and salinity on sections across the flow. As seen in Figure 4, the deep flow at the sill through the Sangihe Ridge is

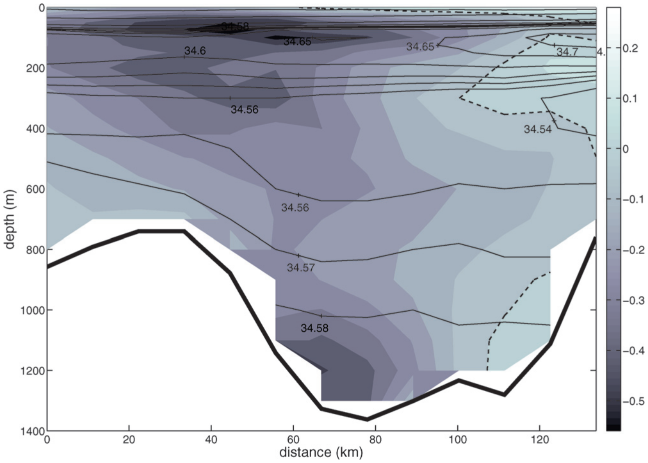

Figure 4. Isotachs of normal velocity (gray colors) and isohalines (solid lines) at the north Sangihe Ridge section (at $i = 156$). Distances along the ridge are shown in the x-axis. The sill located at ~60–100 km is the deepest connection between the Pacific Ocean and the Sulawesi Sea. Velocities are in m/s. The broken line is the 0.0 m/s isotach. The western route section (Figs. 2b and 3b) passes through this section at $j = 223$. See Figure 1 for i, j coordinates.

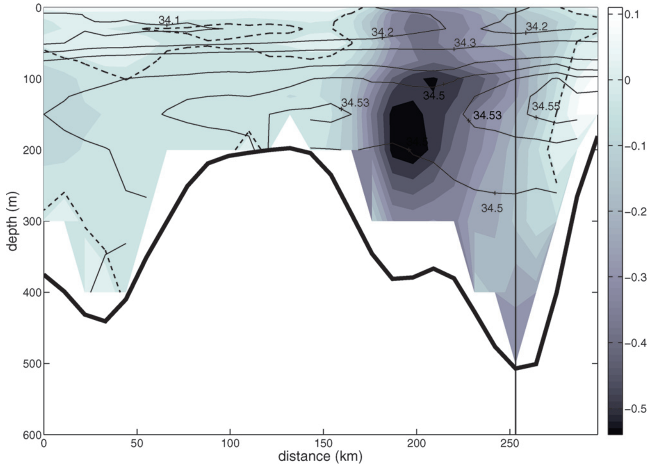

Figure 5. The same as Figure 4 but for the Dewakang section ($j = 138$) in the Makassar Strait (see Fig. A.1). The vertical line shows the location of the section through the Dewakang sill ($j = 50$) presented in Figure 7. The western route section (Figs. 2b and 3b) passes through this section at $i = 57$. See Figure 1 for i, j coordinates.

directed westward. The highest salinity found above the sill is $S \sim 34.58$. Figure 3b clearly shows the effect of the overflow with $S > 34.57$ along the downstream slope of the sill into the Sulawesi Sea, filling the basin below 3000 m. The next barrier is the Dewakang Sill. Profile I (South Makassar Strait) is fresher than J (Flores Sea) at all depths below 500 m. Figure 5 shows the strong southward flow of thermocline water with $S = 34.5$-34.55 across the Dewakang Sill into the Flores Sea. Additionally, the relatively strong southward flow above sill depth of $S = 34.5$ is seen. However, unlike the overflow at the Sangihe Ridge, this water is too fresh to form deep Flores Sea water, but, again, the blocking effect of the sill is quite obvious. Profiles K and F (Banda Sea) are saltier than J. Figure 3b shows that the Flores Sea deep basin has salinity $S > 34.58$ which can be explained only by the penetration of saltier water from the Banda Sea, as was indicated by Gordon *et al.* (1994); Top *et al.* (1997); and Gordon *et al.* (2003). This assumption is confirmed by the cross-section through the Flores-Banda Ridge (Fig. 6) showing the deep westward flow in the south (at 50 km) and center (at 150–250 km) with salinity $S \sim 34.58$-34.59. As in the case of θ, the distribution of salinity in the deep layers of the western Banda Sea demonstrates that saltier waters, relative to the Flores Sea, can come from the Banda Sea only. This fact substantiates the statement, based on the analysis of temperature distribution, that deep Banda Sea water is not formed along the western route but must be supplied from elsewhere.

Finally, we provide Figure 7 to show that the entire water column in the vicinity of the Dewakang Sill moves across the sill from north to south without any return flows.

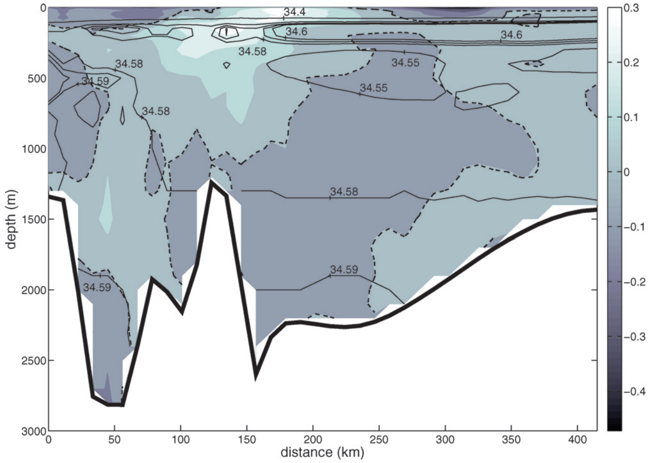

Figure 6. The same as Figure 4 but for the Flores-Banda section ($i = 78$) from the Sunda Arc in the south to south Sulawesi Island in the north. The western route section (Figs. 2b and 3b) passes through this section at $j = 110$. See Figure 1 for i, j coordinates.

3. The analysis of temperature and salinity distributions along the eastern thermocline route

The eastern routes begin at the NGCC port, through which SPW enters the region. Part of this water leaves the region through the NECC port while the remainder enters the Indonesian seas proper either through the Halmahera Sea or by flowing to the north around Halmahera Island into the Morotai Basin and then into the Maluku Sea. Almost all the thermocline flow enters through the Halmahera Sea above sill depth, though there is a trace of thermocline

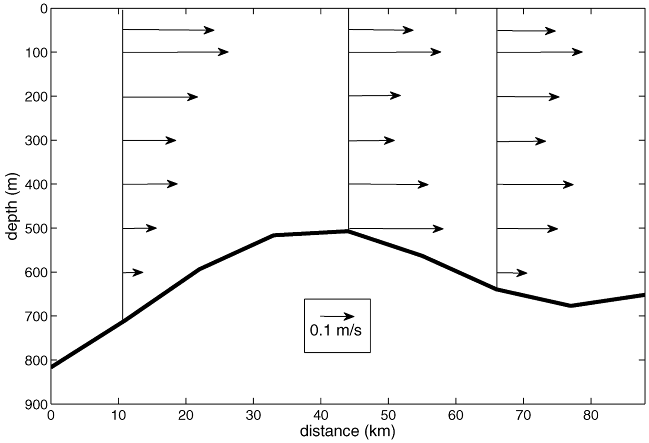

Figure 7. v-velocities in m/s at the section through the Dewakang sill ($i = 50$) from the north (left) to the south (right). See Figure 5 for the location of this section. See Figure 1 for i, j coordinates.

SPW entering the Maluku Sea around Halmahera Island. Deep water flows around Halmahera Island, through the Morotai Basin, Maluku Sea and across Lifamatola Passage into the Seram Sea from where both flows enter the Banda Sea. Finally, Banda Sea water exits the region through the Ombai Strait and Timor Passage. Therefore, the circulation in the Seram Sea is very important and will be considered separately (see Section 4). Consider now the eastern thermocline route, $LMND$, see Figure 1 (the eastern deep route, $LBCDEF$, is analyzed in Section 5). Temperature profiles L and M are very similar throughout the water column to a depth of 3000 m (Fig. 8a). Profile N (Halmahera Sea) diverges from profile M

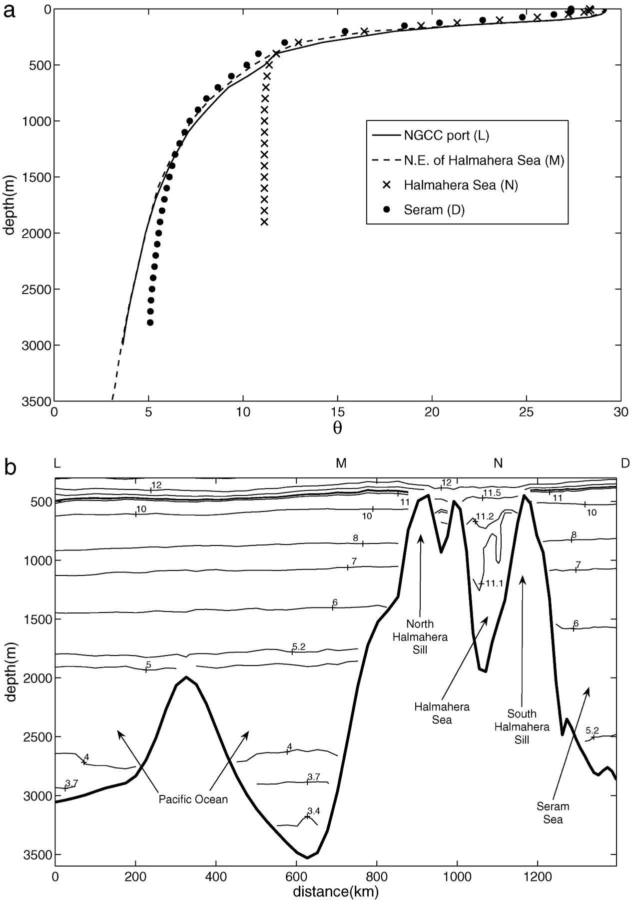

Figure 8. (a) Vertical profiles of potential temperature along the thermocline eastern route for August at points L, M, N, and D. Locations of profiles are indicated in Figure 1 and at the top of Figure 8b. (b) The distribution of potential temperature on vertical section $LMND$ below 300 m (see Fig. 1). The bottom topography along this section is shown. Locations of points L, M, N, and D are indicated along the top of the figure. Distance from point L is shown on the x-axis. Geographical names and locations are shown (see also Fig. A.1).

below 500 m due to the northern Halmahera Sill of depth ~500 m, below which the temperature of profile N is warmer than M, demonstrating the blocking effect of the sill. Profile D (Seram Sea) diverges from N at the depth of the southern Halmahera sill (~500 m). But the temperature of profile D is colder than that of N (Halmahera Sea), illustrating the blocking effect of the south Halmahera Sill and suggesting that the deep Seram basin is not filled across the southern Halmahera Sill. This blocking effect is further demonstrated in the temperature section through the route (Fig. 8b). So the deep Halmahera basin is isolated from the Pacific Ocean to the north and from the Seram Sea to the south by the northern and southern sills (of about the same depth), respectively. The analysis of salinity will show that the Halmahera basin is filled from the Pacific Ocean across the north Halmahera Sill. Also, note that profile D is warmer than L and M below 1400 m and we will show in the next section that this is due to the blocking effect of the Lifamatola Sill.

The analysis of salinity profiles gives some additional information about dynamical processes in this area (Fig. 9a). First, we see a strong salinity maximum of $S = 35.53$ in profile L located at ~150 m with a weak minimum below 1000 m. This structure is characteristic of SPW. The maximum is reduced slightly to $S = 35.36$ at profile M to the north of the Halmahera Sea and sill. Profile N shows that the maximum is reduced to $S = 34.83$ in the Halmahera Sea at 150 m. The maximum at profile D is further reduced to $S = 34.75$ but is most certainly of SPW origin since it is too salty to have a North Pacific source. This rather dramatic decrease in S_{max} is due to increased mixing in the upper layer over the northern sill of the Halmahera Sea (see O'Driscoll, 2007).

Below 500 m the value of salinity in the Halmahera Sea (profile N) is greater than that of the Pacific Ocean to the north (profile M) and the Seram Sea to the south (profile D). So, the Halmahera Sea is filled from the Pacific Ocean since the Seram Sea is too fresh above sill depth (see also salinity section Figure 9b). Additionally, we see the value of salinity in the Seram Sea decreases with depth (see profile D in Fig. 9a and Fig. 9b). In the next section we show that the Seram Sea is filled below ~1000 m by the overflow across the Lifamatola Sill. Seram Sea water has $S \sim 34.65$ at a depth of 500 m decreasing to $S \sim 34.62$ at 1000 m which is too salty to have come from the Maluku Sea across Lifamatola. Indeed, the flow is weakly northward across the Lifamatola Sill into the Maluku Sea at depths ~ 400–1200 m (see Figs. 11 and 12) while the flow into the Seram Basin is westward between Seram and Obi (Fig. 10), so the Seram Sea must be filled down to a depth of 1000 m by thermocline SPW flowing across the south Halmahera Sill into the Seram Sea. This issue is discussed further in the next section.

4. The circulation in the Seram Sea

The circulation in the Seram Sea appears to be composed of 4 major layers: 0–500 m; 500–1200 m; 1200–2000 m; and 2000 m - bottom. Consider the Seram-Obi section (Fig. 10). The flow in the upper 500 m of the Seram Sea is westward. This flow advects SPW with $S_{max} = 34.75$ *into* the Seram Sea from the Halmahera Sea. The major part of this flow

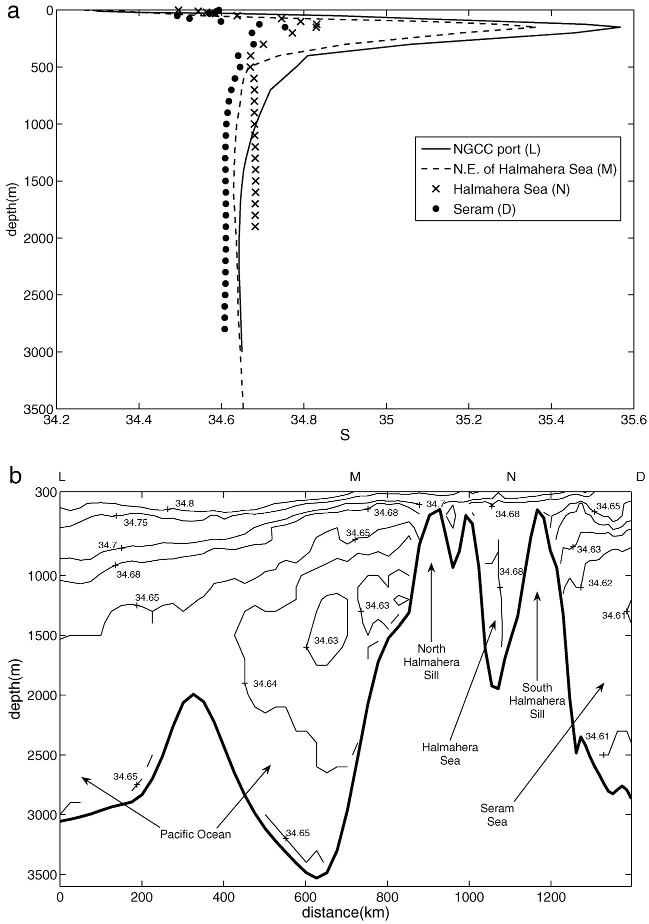

Figure 9. (a) Vertical profiles of salinity along the thermocline eastern route for August at points L, M, N, and D. Locations of profiles are indicated in Figure 1 and at the top of Figure 9b. (b) The distribution of salinity on vertical section $LMND$ below 300 m (see Fig. 1). The bottom topography along this section is shown. Locations of points L, M, N, and D are indicated along the top of the figure. Distance from point L is shown on the x-axis. Geographical names and locations are shown (see also Fig. A.1).

enters the Banda Sea through the Buru-Mangole passage (the corresponding figure is not shown, see section location and transport in Fig. 1), see also O'Driscoll (2007). Most of the remainder enters the Maluku Sea as a weak northward current across the Lifamatola Passage also with $S_{max} = 34.75$ (see Fig. 11).

Figure 10 also shows a westward flow of $S = 34.62 - 34.63$ into the Seram Basin between ~600 and 1200 m. Part of this flow enters the Maluku Sea across Lifamatola as a weak northward current (Figs. 11 and 12). The remainder continues to flow westward to the Buru-Mangole passage and contributes to the ITF (not shown).

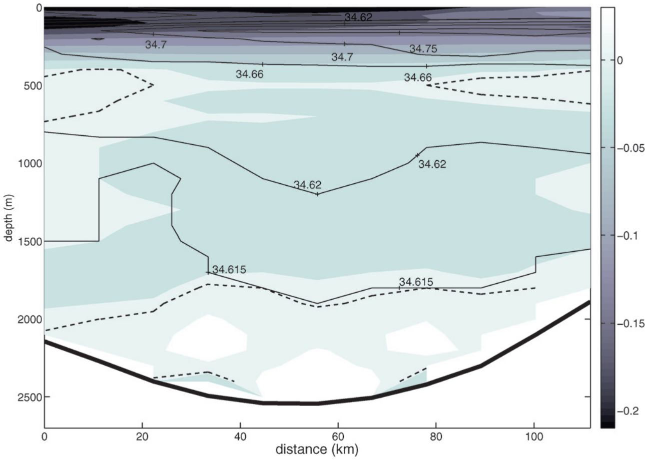

Figure 10. The same as in Figure 4 but for the section between Seram (left) and Obi (right) islands (at $i = 148$). The eastern thermocline route section (Figs. 8b and 9b) passes through this section at $j = 144$. See Figure 1 for i, j coordinates.

At depths between ~1200 m and 2000 m, Figure 10 shows a westward current with $S \sim 34.615$. This water is fresher than lower thermocline SPW above it. Figure 11 shows a deep southward flow across the Lifamatola Sill into the Seram Sea below 1200 m with velocity increasing to a maximum just above the sill. The overflow has salinity $S \sim 34.61$ that fills the deep Seram Sea basin below the sill (see Fig. 9b). It will be shown below (Section 5) that this is SPW.

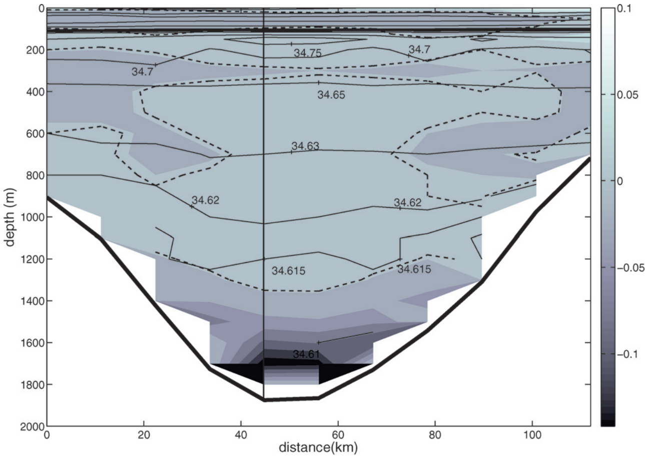

Figure 11. The same as in Figure 4 but for the section across the Lifamatola Sill (at $j = 150$). The vertical line gives the location of the section through the Lifamatola Passage (at $i = 138$) in Figure 12. See Figure 1 for i, j coordinates.

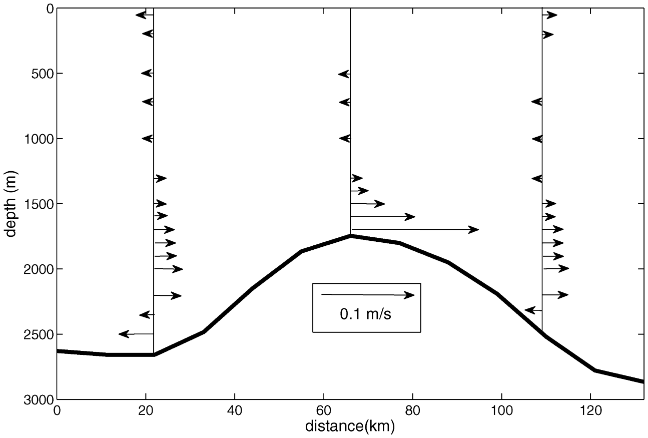

Figure 12. v-velocities in m/s at the section through the Lifamatola passage ($i = 138$) from north (left) to south (right). See Figure 1 for i, j coordinates.

Figure 12 is a north-south section of velocity vectors across the Lifamatola Sill that better illustrates the overflow. There is a return circulation cell below sill depth upstream in the deep Maluku Sea indicating that this basin is not entirely flushed across the sill. We also note the return circulation cell downstream of the sill (giving an indication of strong mixing downstream which is indeed the case and is discussed in O'Driscoll (2007)).

We suggest the following circulation pattern in the deep Seram Sea: the overflow across the Lifamatola Sill turns eastward as it enters the Seram Sea at depths greater than 2000 m (the deep eastward flow is shown in Fig. 10). The flow is blocked when it encounters the shallow depths of the south Halmahera Sill and the passage between Seram and Irian Jaya so it basically upwells and returns westward at ∼1500–2000 m. The flow continues westward across the Seram Sea, spreading to greater depths before entering the Banda Sea at the Buru-Mangole passage. The net flow between Mangole and Buru islands is *out* of the Seram Sea *into* the Banda Sea. It is the flow of water with $S = 34.61$ through the passage between Mangole and Buru that shapes the salinity of the deep Banda Sea.

We argue that the layer between 600 and 1200 m is formed by mixing between thermocline SPW water entering the Seram Sea across the south Halmahera Sill and deeper water entering the Seram Sea across the Lifamatola Sill. It was shown in O'Driscoll (2007) that strong mixing occurs between these two water masses that causes thermocline water to overflow downslope where it mixes with deeper water.

5. The analysis of temperature and salinity distributions along the eastern deep route

In this section we focus on the formation of deep Banda Sea and Seram Sea water due to the overflow across the Lifamatola Sill. We discuss θ and S distributions along the eastern deep route from the Pacific Ocean (profile M), northward around Halmahera Island, through the Morotai Basin and Maluku Sea, and across the Lifamatola Sill into the Seram and Banda seas (section $MBCDEF$, see Fig. 1). It is argued that deep waters overflowing the Lifamatola Sill and filling the deep Seram and Banda seas are mostly of South Pacific origin, in agreement with the studies of Hautala *et al.* (1996) and Wyrtki (1961) (see also Van Aken *et al.* (1988) and Ffield and Gordon (1996)). Additionally, we briefly describe the SPW contribution to Banda Sea thermocline and sub-thermocline (to 1000 m) water.

Beginning with θ profiles along the deep eastern route (Fig. 13a), we see all profiles are essentially the same in the upper 1500 m with slightly warmer surface water (~2°C) at profiles M and B due to their geographic location. Profiles M and B coincide throughout the water column. Profile C is warmer than profile B below 2000 m due to the topographic rise separating the Maluku Sea from the Morotai Basin (see Fig. 13b). Profile D diverges from profile C below 1300 m due to the topography of the Lifamatola Sill. Profile E coincides with profile D throughout most of the water column, deviating slightly below 3000 m due to the topographic rise in the Buru-Mangole passage that separates the deep basins of the Seram and North Banda seas. Profile F is slightly warmer than profile E below 3500 m due to the topographic rise separating the deepest part of the North and South Banda Sea basins. We now analyze the section of temperature along the deep east route (Fig. 13b) to try to shed some light on the reasons for the differences in the temperature profiles. By and large, the flow is from the Pacific Ocean to the Banda Sea. Two features are apparent from the section: the blocking by topographic features of isotherms below the depth of the topographic feature and the filling by upstream waters of the deep basins from the Pacific Ocean (M) to the South Banda Sea (F). Temperatures of ~4°C and less are blocked by the ridge to the east of the Morotai Basin at 600 km in Figure 13b. Temperatures less than ~4.8°C cannot enter the Maluku Sea from the Morotai Basin since these waters are blocked by the topographic rise between the two basins. In the Maluku Sea, $\theta < 4.8°\text{C}$ is blocked by the Lifamatola Sill from entering the Seram Sea. Water above sill depth overflows the sill and fills the deep part of the Seram Sea and Banda Sea downstream with $\theta \geq 4.8°\text{C}$. The sloping isotherms over the sill show that this process extends up to a depth of ~1300 m. So, we have different stratifications downstream and upstream of the sill.

Now, we describe salinity profiles and section along the deep eastern route. Again, Figure 14a shows profile M located to the northeast of the Halmahera Sea and we see the thermocline signature of SPW with $S_{max} = 35.36$ at about 150 m. Profile B shows $S_{max} = 34.8$ at 125 m in the Morotai Basin, profile C shows $S_{max} = 34.76$ in the south Maluku Sea at 125 m, and, again, profile D shows $S_{max} = 34.75$ in the Seram Sea at 125 m. In the Banda Sea, profile E shows a less saline, deeper $S_{max} = 34.63$ at 300 m in the north, while there is no S_{max} at profile F in the south. Recalling that $S_{max} = 34.75$ is advected weakly northward across the Lifamatola Sill, and that NPW has $S_{max} = 34.74$ at the entrance to the model domain at the MC port, it appears that thermocline SPW penetrates into the Morotai Basin directly from the NGCC. Below the thermocline, a minimum is not apparent in profile M. However, a minimum of $S = 34.58$ is seen at 800 m in profile B and

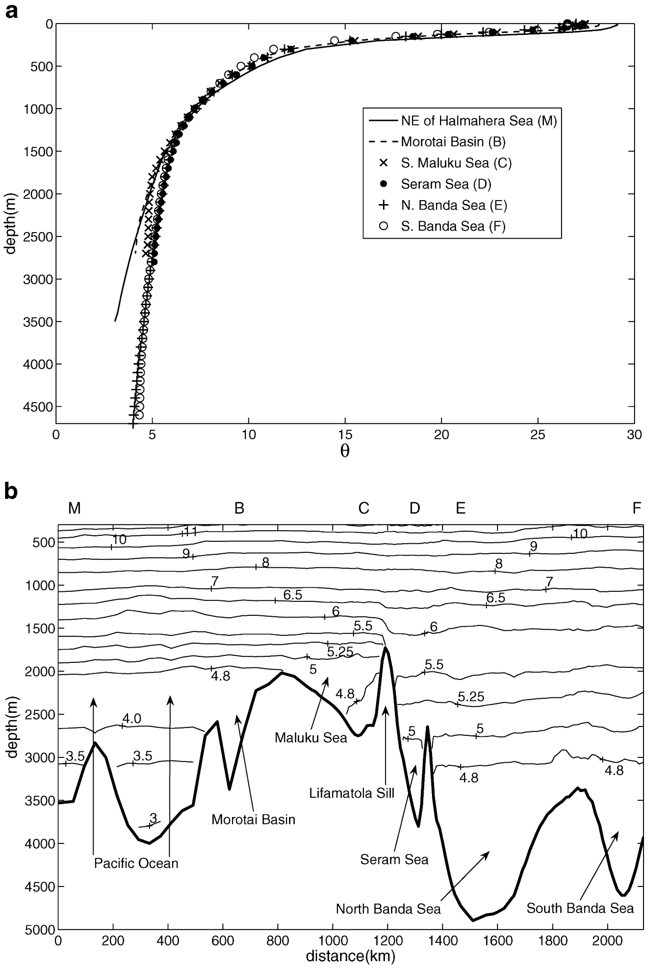

Figure 13. (a) Vertical profiles of potential temperature along the deep eastern route for August at points M, B, C, D, E, and F. Locations of profiles are indicated in Figure 1 and at the top of Figure 13b. (b) The distribution of potential temperature on vertical section $MBCDEF$ below 300 m (see Fig. 1). The bottom topography along this section is shown. Locations of points M, B, C, D, E, and F are indicated along the top of the figure. Distance from point M is shown on the x-axis. Geographical names and locations are shown (see also Fig. A.1).

appears to be, as is shown in the next paragraph, the signature of Antarctic Intermediate Water (AAIW) that enters the model domain at intermediate depths through the southern part of the NECC port. A weak minimum of AAIW is seen in profile C where $S = 34.595$ at 700 m depth. A very weak minimum is seen at profiles D and E, and there is essentially no minimum at profile F in the South Banda Sea. Below the signature of intermediate water, profile B is everywhere fresher than profile M and increases to $S \sim 34.73$ at 2700 m depth.

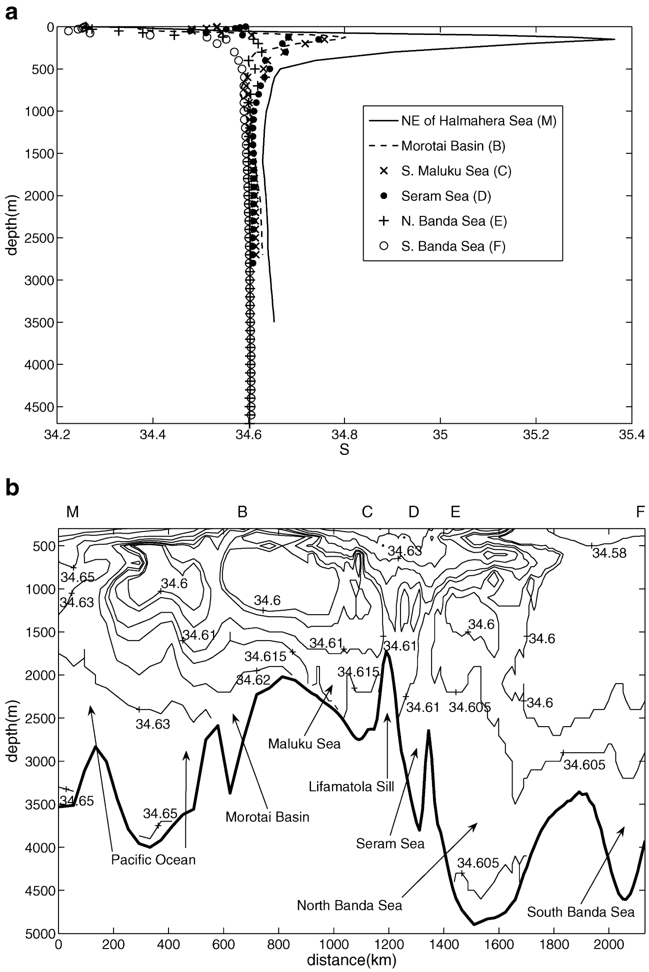

Figure 14. (a) Vertical profiles of salinity along the deep eastern route for August at points M, B, C, D, E, and F. Locations of profiles are indicated in Figure 1 and at the top of Figure 13b. (b) The distribution of salinity on vertical section $MBCDEF$ below 300 m (see Fig. 1). The bottom topography along this section is shown. Locations of points M, B, C, D, E, and F are indicated along the top of the figure. Distance from point M is shown on the x-axis. Geographical names and locations are shown (see also Fig. A.1).

Profile C is fresher than B below 1800 m depth due to the topographic rise between the Morotai Basin and Maluku Sea, and profile D is fresher than C below 1800 m due to the Lifamatola Sill. Profiles E and F are fresher than D and essentially coincide. Figure 14b shows the section of S along the deep eastern route. The signature of AAIW is apparent between the 200 km mark and the Maluku Sea and is approximately contained around the $S = 34.6$ isohaline. As in Figure 13b for temperature, we see the blocking effect of topography and that the deep basins appear to be filled by upstream waters from the Pacific Ocean to the Banda Sea: the $S = 34.63$ isohaline is blocked upstream of the deep Morotai Basin; the $S = 34.62$ isohaline is effectively blocked upstream of the Maluku Sea while $S > 34.61$ is blocked at the Lifamatola Sill. The deep Seram and Banda seas are filled with $S \sim 34.605$, the product of the overflow and mixing with fresher, shallower water at the Lifamatola Sill.

Next, we try to find the *source* of the deep overflow at the Lifamatola Sill. The analysis so far leads us to think that this water is mostly composed of SPW and we will argue this to be the case. We begin by describing properties of velocity vectors, temperature and salinity, respectively, at 1700 m, Figures 15a,b, for the northeast quadrant of the model domain. Figure 15a shows that $S = 34.64$ enters the model domain through the NGCC port and flows westward along the northern coast of Irian Jaya. This is joined by another westward current that enters the model domain through the southernmost part of the NECC port with $S = 34.61$-34.62. The general direction of these currents is shown by the heavy broken arrows in the figure and they advect this relatively salty water northward along the coast. Note these currents have been observed farther east along the coast at 146E, see Firing *et al.* (1998). The two currents merge at the northern tip of Irian Jaya and turn to the north at the north Halmahera Sill and along the east coast of Halmahera Island. From here the current enters the Morotai Basin with $S \sim 34.62$. From the Morotai Basin, part of the flow enters the Karakelong Basin through the two deep connections between the basins, and flows out in the north of the Karakelong Basin, setting up an anti-cyclonic gyre around the Karakelong Ridge. The water entering the Maluku Sea has $S \sim 34.61$ and flows southward across the Lifamatola Sill. The third heavy broken arrow shows the general route of flow from the Morotai Basin to the Maluku Sea. $S = 34.59$ enters the model domain through the MC port at 1700 m. NPW cannot enter the Karakelong Basin at its northernmost passage since there is an outward (eastward) flow of $S = 34.6$ there. However, some NPW can enter the northern edge of the anti-cyclonic gyre, adding this brand of water to the deep route. The argument in Figure 15b is similar to that for Figure 15a and we see that NPW is too cold to enter the Maluku Sea at this depth. However, some NPW may flow into the Maluku Sea within the anti-cyclonic gyre.

To further strengthen our point that it is SPW entering the Seram Sea across the Lifamatola Sill, we present isohalines and isotachs of normal velocity at several sections between the open ports and the Maluku Sea that clearly show the deep water route. Finally, we present a θ-S diagram for the region. The locations of these sections and the profiles for the θ-S diagram are shown in Figure 16. At the NGCC port (see Fig. 16, section 1), Figure 17 shows that salinity $S = 34.64$ flows into the model domain between basically 1500 and 2000 m. Figure 18 shows that $S = 34.61$ enters the model domain through the southern part of the NECC port below 1000 m (see Fig. 16, section 2) and salinity $S = 34.61$-34.62 enters at 2000 m. This current is located at ~100 km from the southern end of the NECC port. Note, again, these currents have been observed further east at $146E$ by Firing *et al.* (1998). Figure 19 shows that $S = 34.59$ is carried into the model domain through the MC

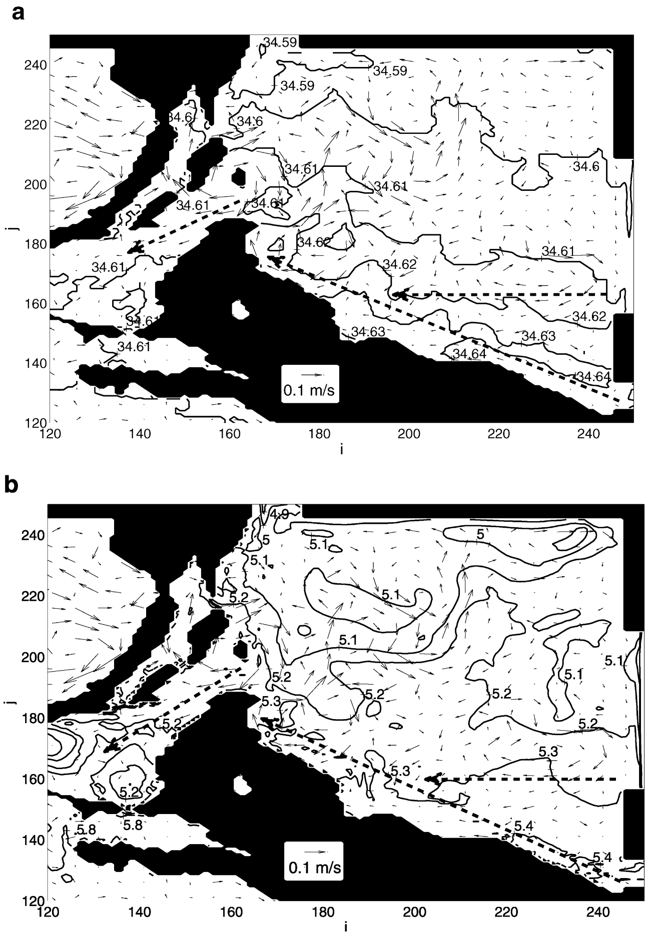

Figure 15. Map of velocity vectors and isohalines at 1700 m depth in August for the northeast quadrant of the model domain (a), and the same map with isotherms replacing isohalines (b). Three open ports are seen in the Pacific Ocean; the Mindanao Current Port (MC) in the north, and the North Equatorial Counter Current Port (NECC) and New Guinea Coastal Current (NGCC) in the east. The heavy broken arrows show the general direction of currents entering the model domain through the NGCC and the south NECC ports, respectively, and the flow into the Maluku Sea from northeast of Halmahera Island.

port at 1700 m, $S = 34.6$ flows in at 2000 m and $S = 34.61$-34.62 enters at $\sim$2500 m (Fig. 16, section 3). Figure 20 is a south-north section from northern Irian Jaya in the south to the northern edge of the model domain (Fig. 16, section 4). $S = 34.63$ flows westward between 1500 and 2000 m in the southern part of the section just north of Irian Jaya and is the continuation of the current entering through the NGCC port, while $S = 34.64$ flows westward below 2500 m. Farther north, in the middle of the section at around 400–500 km

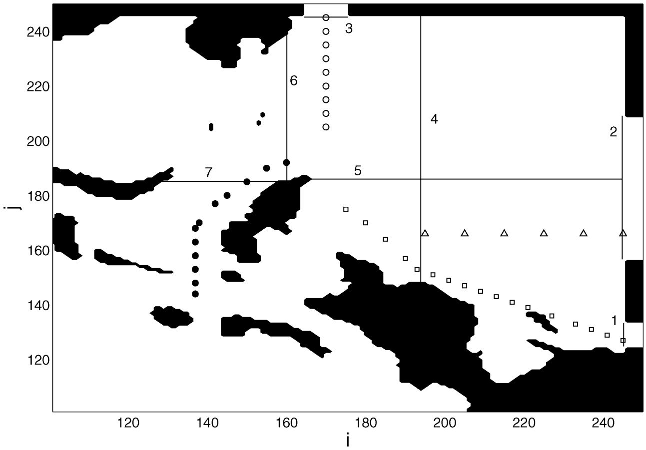

Figure 16. Map of the northeast quadrant of the model domain. Lines with numbers show sections where isohalines are plotted with isotachs of normal velocity in Figures 17–23, including the three Pacific open ports. The symbols show locations of profiles used in the θ-S diagram given in Figure 24.

north of Irian Jaya, $S = 34.61$ flows westward between 1500 and 2000 m and is the continuation of the current entering through the southern part of the NECC port. Figure 21 presents a section from the northeastern tip of Halmahera Island in the west to the southern NECC port in the east (Fig. 16, section 5). Here we see the strong northward flow of $S = 34.61 - 34.63$ between 1500 and 2500 m in the west of the section, 100 km east

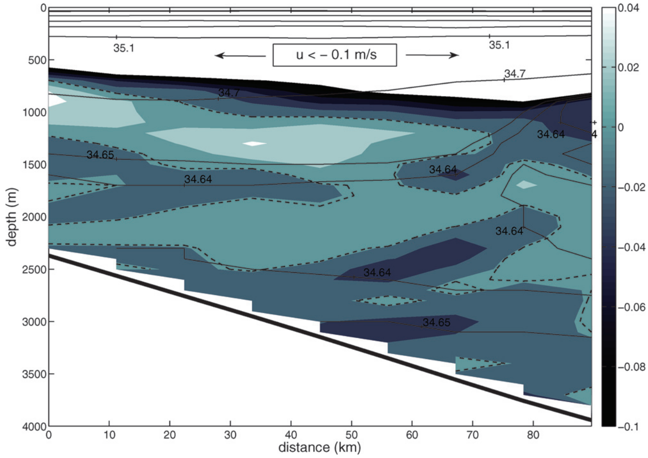

Figure 17. The same as Figure 4 but for the NGCC port section (line 1 Fig. 16). Areas with normal velocities u < −0.1 m/s are shown by arrows.

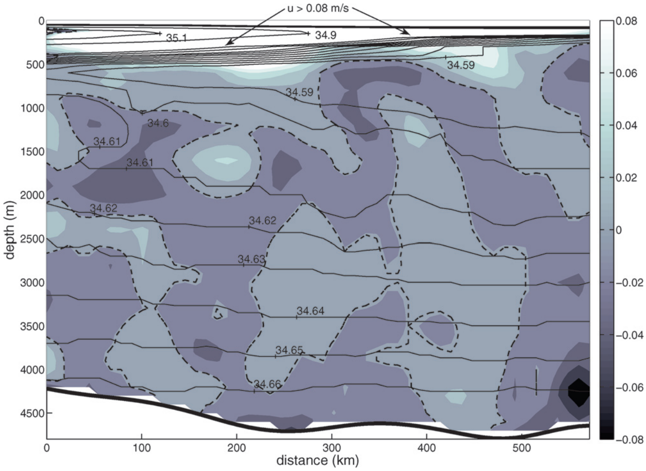

Figure 18. The same as Figure 4 but for the NECC port section (line 2 Fig. 16). Areas with normal velocities u $>$ 0.08 m/s are shown by arrows.

of Halmahera Island. At this stage the westward currents from the NGCC and southern NECC have merged into one northward flow. Figure 22 presents a south-north section from Halmahera to Mindanao (Fig. 16, section 6). Here, we see the relatively strong westward flow of $S = 34.61$ between 1500 and 2000 m and $S = 34.62$–34.63 below 2000 m at about 100 km north of Halmahera Island that is the continuation of the northward flow shown in Figure 21. NPW of $S = 34.59$-34.60 flows westward at 100 km south of Mindanao and

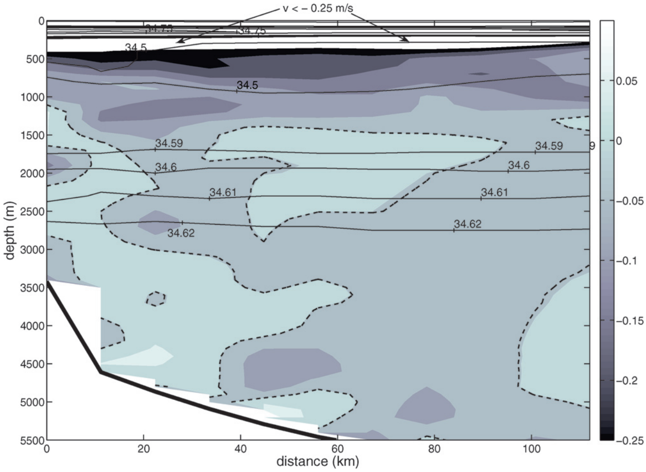

Figure 19. The same as Figure 4 but for the MC port section (line 3 Fig. 16). Areas with normal velocities v < -0.25 m/s are shown by arrows.

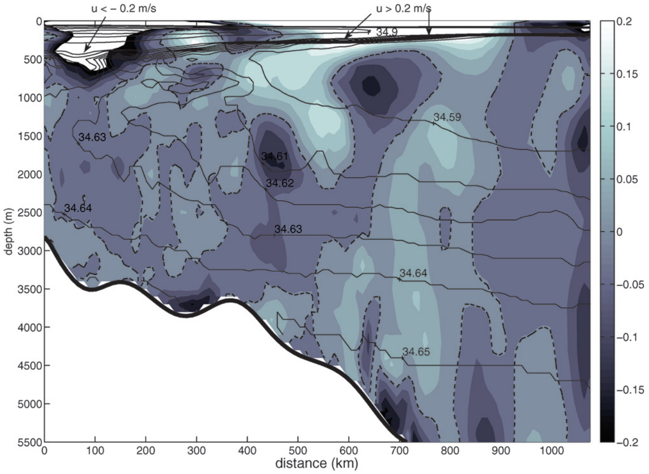

Figure 20. The same as Figure 4 but for the section north from New Guinea (at $i = 193$, line 4 Fig. 16). Areas with normal velocities u < -0.2 m/s and u > 0.2 m/s are shown by arrows.

returns strongly eastward at 200 km south of Mindanao just to the north of the seamount. Figure 23 provides a section across the entrance to the Maluku Sea from the eastern tip of Sulawesi in the west to Halmahera (Fig. 16, section 7). Here, we see the southward flow into the Maluku Sea of $S = 34.61$–34.62 between 1500 m and 2000 m which is the continuation of the flow entering the Morotai Basin from the east. Finally, we present a

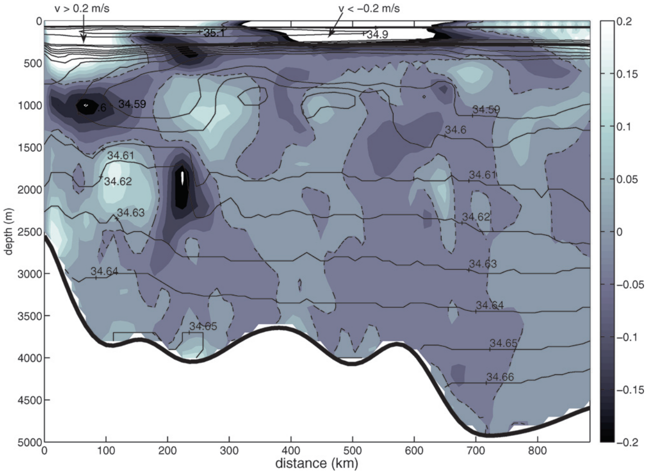

Figure 21. The same as Figure 4 but for the section east from Halmahera Island (at $j = 188$, line 5 Fig. 16). Areas with normal velocities v < -0.2 m/s and v > 0.2 m/s are shown by arrows.

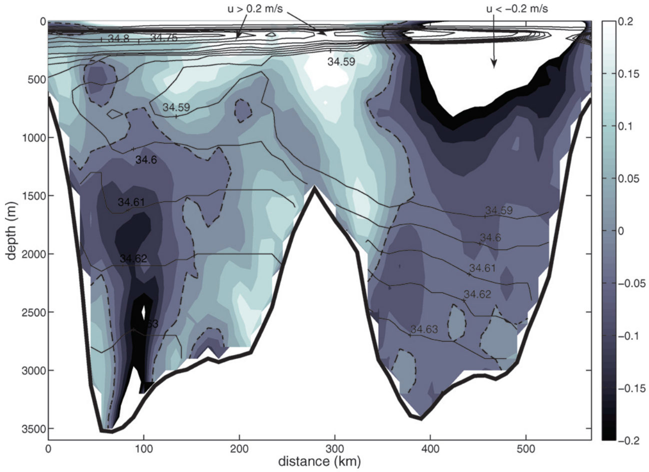

Figure 22. The same as Figure 4 but for the section north from Halmahera to Mindanao (at $i = 160$, line 6 Fig. 16). Areas with normal velocities u < -0.2 m/s and u > 0.2 m/s are shown by arrows.

θ-*S* diagram in Figure 24 showing characterisitics of Maluku Sea and Pacific Ocean source waters within the range of θ and *S* for the overflow. In the range shown, Maluku Sea salinity increases almost linearly with decreasing temperature. NPW is mostly fresher and cooler than Maluku Sea and we see the salty signature of SPW. It appears that Maluku water has mostly the θ-*S* characteristics of SPW with lesser characteristics of NPW.

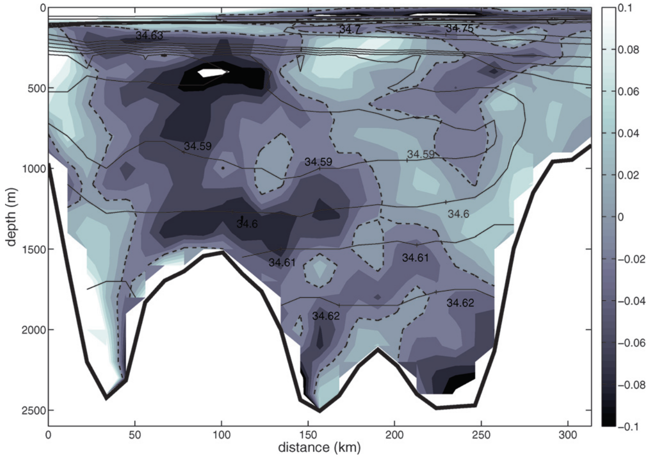

Figure 23. The same as Figure 4 but for the east-west section in the north Maluku Sea from north Halmahera Island (right) to the eastern tip of Sulawesi (left) (line 7 Fig. 16).

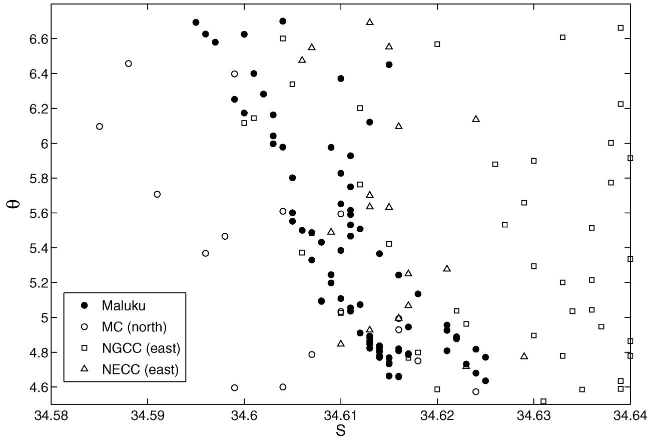

Figure 24. θ-S diagram for the northeast quadrant of the model domain for $\theta = 4.5-6.8$°C and $S = 34.58-34.64$. Profile locations are shown in Figure 16.

6. Seasonal variability

There are no substantial structural changes in potential temperature, θ, and salinity, S, distributions between seasons, though values of some parameters of these distributions (e.g., magnitudes of maxima and minima) can change. The comparison of corresponding profiles shows that seasonal variability is greatest near the surface. Surface temperature changes seasonally by up to ~2°C in the northernmost and southernmost regions but these changes are less pronounced away from these regions. Seasonal changes in surface salinity are generally greatest near land, particularly in the Makassar Strait region and around the Halmahera and Seram seas. In the thermocline, temperature changes on the order of ~0.5°C occur, while isotherms can be vertically displaced by several tens of meters. Salinity extrema generally have similar values throughout the year but they can be vertically displaced. Strong raising and lowering of isohalines, generally associated with topography, is usually seen throughout the year. Below the thermocline, blocking of some isotherms and isohalines is observed throughout the year. Velocity values across the major deep overflows vary little by season but there is some change in the magnitude and extent of deep downwelling and upwelling cells that may explain the displacement of deep isotherms and isohalines (see O'Driscoll (2007) for details). The following comparisons refer to results in February and all changes are considered relative to August unless otherwise stated.

The structure of θ profiles along the western route does not change seasonally. Temperature change is greatest in the upper mixed layer ranging from an increase of ~1.5°C at the MC port to a decrease of ~1.5°C in the south Banda Sea. In the thermocline, there is very little seasonal variability at the MC port and in the Banda Sea. A comparison of temperature sections shows that isotherms within the thermocline are raised by ~10–20 m between the MC port and the Sangihe Ridge. Between the Sangihe Ridge and the Dewakang Sill the isotherms are lowered by ~10–20 m in the upper thermocline while they are raised by ~20–50 m in the lower thermocline. In the west Banda Sea isotherms within the upper thermocline are raised by ~20 m and in the lower thermocline are lowered by ~50 m. In deep water, some notable vertical seasonal displacement of isotherms occurs. In the Sulawesi Sea isotherms are raised by ~50 m down to 1500 m depth, while they are displaced upwards by ~100 m below this depth.

The salinity upper mixed layer is ~100 m deep between Sangihe and Dewakang with $S < 34.2$ which is both deeper and fresher than August (depth ~50 m, $S = 34.2 - 34.4$). The S_{max} of NPW extends from the MC port only as far as the north of the Makassar Strait, unlike August when it extends to the Dewakang Sill. However, remnants of the August S_{max} are seen as patches in the Makassar Strait. The structure of the S_{min} does not change. In deep water, isohalines are raised by several hundred meters in the Sulawesi, Flores and Banda seas.

Along the eastern thermocline route, the upper mixed layer is cooler by ~1°C and shallower (50 m; 100 m in August) at the NGCC port, while it is warmer by ~2°C in the Seram Sea. Isotherms practically coincide in the upper thermocline, while isotherms are raised by ~20–50 m in the lower thermocline in both the Pacific Ocean and Seram sea sides. Salinity structure is similar in all seasons along the eastern thermocline route. The main difference is that the S_{max} is slightly saltier as it crosses the Halmahera Sea. It sinks by up to ~100 m at the south sill entrance to the Seram Sea, resulting in a saltier lower thermocline and a fresher upper thermocline in the Seram Sea.

Along the deep eastern route, temperatures in the upper mixed layer in the Maluku, Seram and Banda seas increase by ~2°C, while layer depth remains constant at ~50 m. In the thermocline, seasonal variability is greatest in the Banda Sea and the Morotai Basin where water is warmer by more than 0.5°C and isotherms are deeper by 20–50 m. The Maluku Sea thermocline is cooler where isotherms are generally raised by ~20–50 m. In deep water, isotherms are generally displaced downwards by ~50 m all along the section in the Morotai Basin, Maluku Sea, Seram Sea, and Banda Sea. Salinity structure along the deep eastern route is essentially the same during all seasons. The major difference is the reduced value and the increased depth of the S_{max} entering the Maluku Sea across the Lifamatola Sill and is due to the sinking of the S_{max} as it crosses the south Halmahera Sill mentioned previously. There is no change in salinity structure from the eastern side of Halmahera through the Morotai Basin.

7. Comparison with observations

In general, the developed model correctly reproduces the basic features of observed potential temperature and salinity distributions. We consider now in detail results of the comparison of simulated and observed data.

We begin with the western route. Essentially, there is satisfactory agreement between the simulated and observed (Gordon *et al.*, 2003) estimates of the effective depths of topographic features (the effective depth is the depth of the threshold isoline upstream of the obstacle). There is a good fit of observed to simulated features such as the location of the salinity maximum of $S \sim 34.75$ and minimum of $S \sim 34.48$ at ~125 m and ~300 m respectively and the lower boundary of the thermocline at ~250 m in the north Makassar Strait (profile H); the location of the salinity maximum of $S \sim 34.61$ at ~100 m and minimum of $S \sim 34.53$ at ~400 m, and the lower boundary of the thermocline at ~300 m in the Flores Sea (see Gordon, 2005; Fig. 4). However, simulated deep temperatures of $\theta \sim 4.5$°C in the East Sulawesi Sea (profile G) and $\theta \sim 2.5$°C in the MC port region (profile A) are slightly higher than observed; in contrast, the corresponding simulated salinities of $S \sim 34.58$ and $S \sim 34.65$ are slightly lower than observed (see Gordon *et al.*, 2003; Fig. 2). This problem is discussed in the Appendix, Section d.

In shallower waters in the Makassar Strait and the Flores Sea, the model results are very similar to the data of Ilahude and Gordon (1996; Fig. 3). For salinity, the simulated results agree with data at depth provided by Gordon *et al.* (2003; Fig. 5b), where the deep Makassar Strait and southwest Sulawesi Sea are fresher than the Flores Sea which in turn is fresher than the western Banda Sea. In shallower waters, the position of isohalines characterizing the salinity maximum and minimum along the Makassar Strait are satisfactorily reproduced by the model (Gordon *et al.*, 2003; Fig. 5b; Ilahude and Gordon, 1996; Fig. 3). The same is true for the low salinity cell over the Dewakang Sill seen in Ilahude and Gordon (1996; Fig. 3). The weaker maximum seen in February in Gordon *et al.* (2003; Fig. 5b) and Ilahude and Gordon (1996; Fig. 3) is also reproduced by the model. The relatively weak salinity maximum and minimum in the Flores Sea observed by Gordon *et al.* (1994; Fig. 4) and the absence of salinity extrema in the western Banda Sea (Gordon *et al.,* 2003, Fig. 5b; Gordon *et al.,* 1994, Fig. 4; Ilahude and Gordon, 1996, Fig. 4) are adequately displayed by the model.

Along the thermocline eastern route, we find an effective sill depth across the northern Halmahera Sill of ~500 m, somewhat less than ~600 m observed by Gordon *et al.* (2003; Fig. 2). As a result, the model temperature at depth within the Halmahera Sea is warmer than observed (see also Cresswell and Luick, 2001), while the simulated temperature difference in profiles M and N match the observed difference below the effective depth of the sill. For the deep Halmahera Sea, the model gives salinity of $S \sim 34.66$, more than the observations of Gordon *et al.* (2003, Fig. 2) who found $S \sim 34.60$ (see also Van Riel, 1943). The fact that the model effective depth of the North Halmahera Sill is less than observed appears to be the main reason for the relatively warmer and saltier deep water seen in the model in the deep Halmahera Basin.

Along the deep eastern route, the model profile in the south Maluku Sea (profile C) gives salinity maximum of $S \sim 34.76$ at ~150 m, in good agreement with that seen in Gordon (2005; Fig. 4). The same is true for the model salinity minimum of $S \sim 34.595$ at ~700 m and model salinity of $S > 34.61$ below ~1700 m (compare with Gordon *et al.*, 2003; Fig. 2). In the Seram Sea (profile D), the model gives a salinity maximum in August of $S \sim 34.75$ at ~150 m, in contradiction to observations (Gordon, 2005; Fig. 4). But below this maximum the model salinity decreases to a deep value of $S \sim 34.61$ below ~1500 m, in very good agreement with Gordon *et al.* (2003; Fig. 2). The salinity maximum seen at profile D is much reduced in February and is not apparent in November and May, in close agreement with observations. In the south Banda Sea (profile F), the model shows no salinity extrema in agreement with observations of Gordon (2005; Fig. 4). The deeper salinity of $S \sim 34.61$ also agrees with observations of Gordon *et al.* (2003; Fig. 3). Comparing temperatures at depth between the south Maluku Sea (profile C) and the Seram Sea (profile D) gives a simulated effective Lifamatola Sill depth of ~1500 m, in good agreement with the effective depth of ~1650 m found by observations (Gordon *et al.*, 2003).

Comparing θ- and S-sections along the deep eastern route, we see that the temperature structure in the upper ocean agrees with that of Gordon *et al.* (2003; Fig. 6a). At depth, the model shows that isotherms slope down over the Lifamatola Passage into the Seram Sea, and even into the Banda Sea, and that the deep waters of the south Maluku Sea are much cooler than deep waters of the Seram and Banda seas, in accord with Gordon *et al.* (2003; Fig. 6a) and Van Aken *et al.* (1988; Fig. 9). For salinity at depth, the model isohalines slope downward across the Lifamatola Passage and that is why the deep south Maluku Sea appears saltier than the Seram and Banda seas, again in agreement with Gordon *et al.* (2003; Fig. 6b). The Banda Sea has almost constant salinity at depth also in accord with Gordon *et al.* (2003; Fig. 6b) and Van Aken *et al.* (1988; Fig. 10). In the upper ocean, the model shows no salinity extrema in the south Banda Sea, corresponding well with the data of Gordon *et al.* (2003; Fig. 6b). In the south Maluku Sea, both model minimum and maximum were observed by Gordon *et al.* (2003; Fig. 6b). In the north Maluku Sea the model salinity extrema have also been observed by Ilahude and Gordon (1996; Fig. 5).

8. Conclusions

The influence of bottom topography on the distribution of temperature and salinity in the Indonesian seas region has been studied with a high-resolution model based on the Princeton Ocean Model. One of the distinctive properties of the model is an adequate reproduction of *all* major topographic features in the region by the model bottom relief. Topographic elevations break the Indonesian seas region down into separate basins. The connections between these basins are basically conducted through sills and narrow passages. Both shallow sills, e.g., Dewakang Sill, south and north Halmahera Sills, and deep sills, e.g., Sangihe Sill and Lifamatola Sill, are observed in the region. This topography substantially impacts the distribution of potential temperature and salinity in the region. The Banda Sea is of particular importance: it is the main source of water exiting the region toward the Indian Ocean through the Ombai Strait and Timor Passage. Estimates of simulated transports through the Indonesian seas show substantial contributions from deep parts of the Banda Sea to the transports of heat and salt between the Pacific and Indian oceans.

The difference in potential temperature, θ, and salinity, S, distributions in adjacent basins is primarily due to specific properties of advection of θ and S across a topographic rise. By and large, the topographic rise blocks deep flow between basins whereas water shallower than the depth of the rise is free to flow between basins. To understand this process, we analyze the structure of simulated fields of temperature and salinity. The flow goes across the sill. To identify a range of advected values of θ or S we consider special sections over the sills with isotherms or isohalines and isotachs of normal velocity. Both types of section have been analyzed, but, for brevity, we have provided in the paper only sections with isohalines and isotachs of normal velocity. Salinity appears to be a more informative tracer than potential temperature. By using this tool we identify the impact of various topographic rises on the distribution of θ and S.

To analyze the influence of bottom topography in detail we have considered the three major routes of flow of Pacific water through the Indonesian seas, which have been identified as western, eastern thermocline and eastern deep routes. The western route follows the flow of North Pacific Water (NPW) through the Sulawesi Sea, Makassar Strait and Flores Sea. This is the main branch of the Indonesian Throughflow (ITF). The distribution of both deep θ and S is very different in the Pacific and Sulawesi Sea. The lowest value of θ in the Pacific is 2.6°C, while in the Sulawesi Sea it is 5.25°C. This difference is explained by the blocking effect of the Karakelong and Sangihe ridges that prevent the advection of deep cold and saline water from the Pacific Ocean to the Sulawesi Sea. There is no notable difference in θ and S distributions between the Makassar Strait and Sulawesi Sea. The rather shallow Dewakang Sill with depth ~600 m blocks the advection of $\theta < 8°C$ and salinity $S > 34.55$ from entering the Flores Sea. Therefore, the deep Flores Sea basin is filled from the Banda Sea across the ridge between the Flores and Banda Sea with a depth of roughly 2000 m. The analysis of the western route leads to the conclusion that deep Banda Sea water is not formed along the western route. Further study shows that it is formed from North Banda Sea water. We notice that the same conclusions were made by Gordon *et al.* (2003) by comparing CTD profiles of temperature and salinity in adjacent basins. But it appears that we cannot restrict ourselves to the consideration of profiles only. Based on temperature and salinity profiles (see Figs. 2b and 3b) it is hardly possible to recognize the blocking effect of the Dewakang Sill. This effect can be revealed only by the analysis of advection across the sill (see Fig. 5).

The eastern routes begin at the NGCC port, through which South Pacific Water (SPW) enters the region. Part of this water leaves the region through the NECC port while the remainder enters the Indonesian seas proper either through the Halmahera Sea or by flowing northward around Halmahera Island, then into the Morotai Basin and the Maluku Sea. The deep Halmahera Basin is isolated from the Pacific Ocean to the north and from the Seram Sea to the south by the north and south Halmahera Sills of ~500 m depth, respectively. The Halmahera Basin is filled from the Pacific Ocean across the north Halmahera Sill. Almost all of the thermocline SPW in the Indonesian seas enters the Seram Sea via the Halmahera Sea above sill depth, though there is a trace of thermocline SPW entering the Maluku Sea around Halmahera Island. Deep SPW flows around Halmahera Island, through the Morotai Basin, Maluku Sea and across Lifamatola Passage into the Seram Sea from where both thermocline and deep waters enter the Banda Sea.

The circulation in the Seram Sea appears to be a key point. It is viewed as being composed of four major layers. The flow in the upper 500 m advects South Pacific Water with $S_{max} = 34.75$ *into* the Seram Sea from the Halmahera Sea. The major part of this flow enters the Banda Sea through the Buru-Mangole Passage. Most of the remainder enters the Maluku Sea as a weak northward current across the Lifamatola Passage also with $S_{max} = 34.75$.

There is also a westward flow of $S = 34.62$-34.63 through the Obi-Seram section into the Seram Basin between ~600 and 1200 m. Part of this flow enters the Maluku Sea across Lifamatola as a weak northward current. The remainder continues to flow westward to the Buru-Mangole Passage and contributes to the ITF. This water is formed by mixing of thermocline SPW that enters the Seram Sea across the south Halmahera Sill with deeper water, mostly of SPW origin, that entered the Seram Sea across the Lifamatola Sill. The mixing occurs in the eastern Seram Sea, downslope of the south Halmahera Sill.

A deep southward flow across the Lifamatola Sill into the Seram Sea exists below 1200 m with velocity increasing to a maximum just above the sill. This overflow, with temperature $\theta > 4.8°C$ and salinity $S \sim 34.61$, fills the deep Seram Sea basin below sill depth. We concluded that deep waters overflowing the Lifamatola Sill and filling the deep Seram Sea are mostly of South Pacific origin in agreement with studies of Wyrtki (1961) and Hautala *et al.* (1996) (see also Van Aken *et al.*, 1988 and Ffield and Gordon, 1996). Based on our model simulations we traced the path of SPW from the NGCC port all the way to the Lifamatola Passage. It was shown that water with $\theta = 5.4°C$, $S = 34.64$ enters the model domain through the NGCC port and flows westward along the northern coast of Irian Jaya. This flow is joined by another westward current that enters the model domain through the southernmost part of NECC port with $\theta = 5.2 - 5.3°C$, and $S = 34.61 - 34.62$. The two currents merge at the northern tip of Irian Jaya and turn to the north of the Halmahera Basin and east of Halmahera Island. The current enters the Morotai Basin with $\theta = 5.2°C$ and $S \sim 34.62$. From the Morotai Basin, part of the flow enters the Karakelong Basin through the two deep connections between the Morotai and Karakelong basins, and flows out in the north of the Karakelong Basin, setting up an anti-cyclonic gyre around Karakelong Ridge. NPW cannot enter the Karakelong Basin at its north passage since there is an outward (eastward) flow. However, some NPW can enter the northern edge of this anti-cyclonic gyre around the Karakelong Ridge, contributing some NPW to the deep route. The topographic rise between the Morotai Basin and Maluku Sea blocks the advection of water with $\theta < 4.8°C$ and $S > 34.63$, and, in turn, the Lifamatola Sill blocks the advection of water with $\theta < 4.8°C$ and $S > 34.62$. Similar results, but not as detailed, were published recently by Koch-Larrouy *et al.* (2008).

We argue that the overflow across the Lifamatola Sill, as it enters the Seram Sea, turns eastward at depths greater than 2000 m. The flow is blocked when it encounters the shallow depths of the Halmahera Sill and the passage between Seram and Irian Jaya so it basically upwells and returns westward at ~1500–2000 m. The flow continues westward across the Seram Sea, spreading to greater depths before entering the Banda Sea at the Buru-Mangole Passage. The net flow between Mangole and Buru Islands is *out* of the Seram Sea *into* the Banda Sea. It is the flow of water with $\theta \geq 4.8°\text{C}$ and $S = 34.61$ through the passage between Mangole and Buru Islands that shapes the temperature and salinity of the deep Banda Sea.

There are no substantial structural changes of potential temperature and salinity distributions between seasons, though values of some parameters of temperature and salinity distributions (e.g., magnitudes of maxima and minima) can change. Thus, our conclusions regarding the formation of deep temperatures and salinities in the Seram and Banda seas based on August data remain valid throughout the year.

It is important to stress that the *main structure* of observed distributions of temperature and salinity, namely the monotonic decrease of temperature with depth and the presence of a maximum and minimum in salinity profiles, is reproduced very well by the model throughout the entire domain. In the upper ocean (0–500 m) the model and observed profiles are very similar. In the deeper ocean temperature deviations can reach 1°C while salinity deviations are essentially on the order of several 0.01, although in some layers, e.g., the layer of salinity minimum at the NGCC port, they can reach as much as 0.1.

Acknowledgments. K. O'Driscoll would like to thank the Naval Oceanographic Office for supporting his graduate education. V. Kamenkovich gratefully acknowledges support from the National Science Foundation through grants OCE 96-33470 and OCE 01-18200. The authors would like to express their gratitude to Dmitri Nechaev, John Hunter, Alexander Shchepetkin, and Pat Hogan for helpful suggestions concerning numerical aspects of the model. We are thankful to G. Veronis and anonymous reviewers for their useful comments.

APPENDIX

Model description

The model configuration coincides with that described in Burnett *et al.* (2003; Figs. 1 and 2). The model domain is shown in Figure A.1 along with names of important topographic features and open ports. The domain extends throughout the Indonesian seas region and has 250 × 250 grid cells in the horizontal, identified in Figure A.1 by i and j. The model has horizontal resolution of ~10 km in both i- and j-horizontal directions. The model has four open ports to simulate the impact of major currents entering and exiting the region. The orthogonal curvilinear coordinate system used in the POM has been rotated relative to the latitude-longitude system so that the open port in the Indian Ocean region (IO port) lies on the transect line extending from Java to northwest Australia along which observations were made (see, e.g., Fieux *et al.*, 1994; Sprintall *et al.*, 2000). The ITF exits the model domain and enters the Indian Ocean through this port. There are three open ports in the Pacific region: the Mindanao Current port in the north (MC port); the New Guinea Coastal Current port (NGCC port) just to the north of New Guinea/Irian Jaya; and the North Equatorial

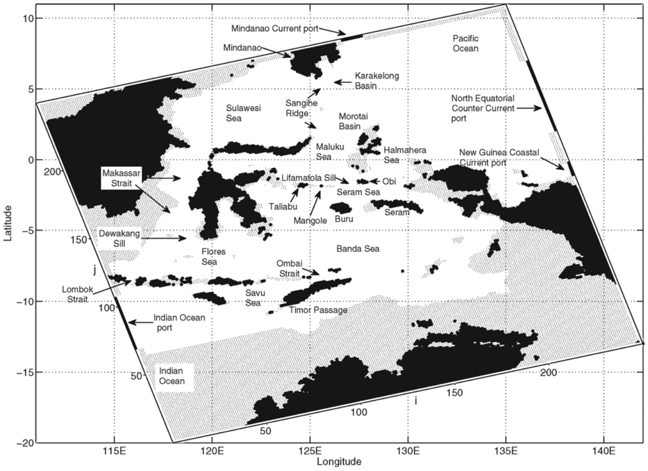

Figure A.1. The model domain location along with names of important topographic features and open ports. The model domain was rotated relative to lines of constant Lat - Lon so that the Indian Ocean port was located on the JADE August 1989 CTD transect between northwestern Australia and Bali. The model (x, y) domain ranges between i and j values of 1 to 250, respectively, (see i, j values along model domain edge). Model domain corners in Lat - Lon values are as follows: SW 20S 118E, SE 13S 142E, NE 11N 135E, and NW 4N 111E. The 4 open ports are shown as bold lines along the edge of the model domain. The depth in the grey (dotted) region is less than 100 m. However, the grey region in the Indian Ocean in the southwestern corner of the model domain is greater than 100 m but has been excluded from the model integration to facilitate the Indian Ocean open port.

Counter Current port (NECC port) in the east. By and large, Pacific waters enter the domain through the MC and NGCC ports and exit through the NECC port. The grey regions in Figure A.1 are shallow (depth is less than 100 m) and are considered as land (see discussion of model topography below). There are 29 σ-levels in the vertical so that important features of the vertical structure are properly resolved over all types of topography.

a. Bottom topography

We used ETOPO5 data base. First, the regions in Figure A.1 with depth less than 100 m are considered as land. The grey area to the southwest of Timor Passage and south of the IO Port that is deeper than 100 m has been excluded from the model integration to facilitate setting the open boundary condition at the port and does not affect conditions at the exit passages, Lombok, Ombai and Timor that are important to the model results. The Torres Strait is closed since it is very shallow, ∼10 m, and does not contribute to the ITF. The connections to the Sulu Sea and the Java Sea have also been closed. Small passages in the Lesser Sunda Island Chain were closed but the important Lombok and Ombai straits were retained. Some local modifications in the topography have been introduced to eliminate excessively large local slopes without changing the structure of the topography. For example, we set the maximum depth in the model domain to 6000 m (e.g., the Mindanao Trench is deeper than 9000 m); set minimum depth of seamounts in the Pacific basin to 2000 m; removed two small islands west of the NGCC port, and so on. Theses changes to ETOPO5 data reduce the difficulty in simultaneously satisfying the POM recommendation for bottom slopes and retaining the main structural features of the bottom topography.

Based on observations, Gordon *et al.* (2003) proposed that during the boreal winter monsoon the wind drives low-salinity Java Sea surface water through the Karimata Strait into the southern Makassar Strait (see also Koch-Larrouy *et al.*, 2008). This effect is not included in our model, since we closed the Karimata Strait. It is hardly possible that this effect changes substantially the estimate of bottom form stress in the model domain and the interaction of NPW and SPW. Tozuka *et al.* (2007, 2009) showed that the incorporation of the Karimata Strait does not have any impact on the deep velocities even in the Makassar Strait.

The modified bottom topography was smoothed following the procedure outlined in Il'in *et al.* (1974). See details in O'Driscoll (2007).

This smoothed topography was used in all numerical experiments. Obviously, there are differences between the smoothed and real topography. Then the question becomes: are our results based on such a smoothed topography reasonable? From our knowledge of the general pattern of the circulation in the Indonesian seas we conclude that the topography in the areas of the Sangihe Ridge, Labani Channel, Dewakang Sill, Halmahera Sea, Lifamatola Passage, Lombok Strait, Ombai Strait, Timor Passage, and the passage between Irian Jaya and Seram Island is critically important. The comparison with the unsmoothed topography showed that the structure of the above mentioned topographic features has been retained. This implies that the basic isobaths are not noticeably displaced after smoothing (e.g., at the Lifamatola Sill, smoothed and unsmoothed 1500 m and 2000 m isobaths practically coincide). The relative rms of deviations between smoothed and unsmoothed depths over the whole domain is 19%, but in many dynamically important areas this error is less. Comparison of simulated transports through major passages with observed values (Section 3) demonstrates a reasonable compatibility (see O'Driscoll, 2007). We did not strive to reproduce all properties of the Indonesian seas circulation with great accuracy. Our goal was to pursue a process-oriented study, rather than to develop an operational forecasting model of the region. Our concern was to retain all important physical processes in the model. So in the model, we have *model* sills, and *model* temperature and salinity. But the simulated fields we study were all consistent to allow us to explore, for example, the role of *model* sills in the formation of *model* deep salinity. That is why our analysis based on simulated fields is meaningful.

To estimate a possible effect of the POM approximation of horizontal pressure gradients (see the discussion of this effect in, e.g., Haney, 1991; Mellor *et al.*, 1994) we ran, as is common practice, some experiments without any external forcing and with distribution of potential temperature and salinity dependent on z only. Deviation of velocities from zero were not substantial.

b. Boundary conditions

i. Boundary conditions for the depth-averaged motion. (1) Specification of the normal velocity based on the prescribed total transport and assumed simple distributions of this velocity across the port. (2) Tangential velocity is equal to zero.

ii. Boundary conditions for the 3D motion. (1) Orlanski's condition with nudging for the normal velocity. Following the recommendations of Marchesiello *et al.* (2001), we have for the Indian Ocean IO port:

$$\begin{aligned}\frac{u^{(n+1)}(2,j,k)-u^{(n-1)}(2,j,k)}{2\Delta t}\\ &= c(j,k)\frac{u^{(n)}(3,j,k)-0.5[u^{(n+1)}(2,j,k)+u^{(n-1)}(2,j,k)]}{\Delta x_j}\\ &\quad - r_{IO}^{(v)}\big[u^{(n-1)}(2,j,k)-u_e^{(n-1)}(j,k)\big],\end{aligned} \tag{A.1}$$

where $c(j,k)$ is calculated according to the POM2K code (see Orlanski, 1976); Δt is the time step; Δx_j is the distance between $(2, j)$ and $(3, j)$ grid points; superscript n indicates the time $n\Delta t$; $r_{IO}^{(v)}$ is the nudging coefficient for the normal velocity u; u_e is the port normal velocity prescribed from observations. This formula is used for the calculation of the boundary value $u^{(n+1)}(2,j,k)$. The nudging coefficient $r_{IO}^{(v)}$ differs for inflow and outflow points, identified by the sign of $u^{(n)}(2,j,k)-c(j,k)$: for outflow points $u^{(n)}(2,j,k)-c(j,k) < 0$ while for inflow points $u^{(n)}(2,j,k)-c(j,k) > 0$. Usually the nudging coefficient for inflow points is larger than for outflow points. Note that by definition $c(j,k) \geq 0$. (2) Tangential velocity is set to zero. (3) Orlanski's conditions with nudging for temperature and salinity. Basically these conditions are similar to (A.1). Similar formulas have been used at the $NGCC$, $NECC$, and MC ports. (4) The turbulence energy and length scale are set to zero.

iii. Specification of the port normal velocity u_e and total port transports. The grid spacing of the Levitus climatology data does not allow for use of the geostrophic relations to specify u_e. Moreover, the NGCC port is located too close to the equator. Therefore, published observations and some modeling results have been used to determine the port normal velocity u_e and total port transports. Based on the available observational data we estimate annual mean, August and February values of port transports and port normal velocity $u_m(z)$, see O'Driscoll (2007; Fig. 2.2). To calculate u_e, used in boundary condition (3), we scale $u_m(z)$ such that the depth integral of it is equal to S_x used in the boundary condition for the external mode

$$u_e(y,z,t) = \frac{u_m(z)}{\int_{-H}^{0} u_m(z)dz} S_x(y,t), \tag{A.2}$$

where $S_x(y,t)$ is the depth-integrated port normal velocity determined by using the specified total transport and assumed simple distribution of velocity across the port.

The detailed analysis of observational data for all ports and calculation of u_m and corresponding S_x is given in O'Driscoll (2007). We supposed that such an approach is more reliable than the use of results of a global OGCM. The area of formation of the NGCC,for example, has such a complicated coastline geometry that it is hardly possible to properly model the circulation in such an area with a global OGCM.

iv. Boundary conditions at the sea surface. The surface boundary condition for the heat equation is as follows:

$$-K_H \frac{\partial T}{\partial z} = \frac{1}{\rho_0 c_p} Q(T) \quad \text{at} \quad z = 0, \tag{A.3}$$

where surface heat flux $Q(T)$ is the sum of longwave radiation, latent heat (evaporation) and sensible heat, ρ_0 is the mean density and c_p is the heat capacity at constant pressure p. Assuming that the model calculated T does not deviate substantially from the climatic value T_{clim}, $Q(T)$ can be represented as (see Ezer, 2000)

$$Q(T) = Q(T_{clim}) + \frac{\partial Q}{\partial T}(T - T_{clim}). \tag{A.4}$$

In the Indonesian seas the contribution of sensible heat to Q is rather small compared to other components. Therefore Q should increase when T is increased (it is obvious for long wave radiation and evaporation). Thus it is reasonable to expect that $\partial Q/\partial T$ is positive. This value is usually estimated as 50 W m^{-2} K^{-1}. Dividing by $\rho_0 c_p$ we introduce $r = 1/(\rho_0 c_p)(\partial Q/\partial T)$ and rewrite condition (A.3) in the form

$$-K_H \frac{\partial T}{\partial z} = Q(T_{clim}) + r(T - T_{clim}) \quad \text{at} \quad z = 0, \tag{A.5}$$

used by Oey and Chen (1992). Taking c_p equal to 4000 Jkg^{-1} K^{-1} and ρ_0 equal to 1000 kg m^{-3} we find r = 1.25×10^{-5} m s^{-1}. Shortwave solar radiation, R, should be added to the rhs of the heat equation in the form

$$-\frac{\partial R}{\partial \sigma} \tag{A.6}$$

where the formula for R is given in the POM code. In this study, we have used the Adjusted Southampton Oceanography Centre (SOC) surface flux climatology (Grist and Josey, 2003). We assume these data can be interpreted as $Q(T_{clim})$. The analogous boundary condition for salinity S can be formulated by introducing the freshwater flux. But this quantity is very poorly known in the Indonesian seas area, so we have specified the salinity at the surface

$$S = S_{clim} \quad \text{at} \quad z = 0. \tag{A.7}$$

Surface monthly climatological salinity S_{clim} is taken from Levitus climatology (Conkright *et al.*, 2002). To take into proper consideration mixing processes in the upper and deep layers, nudging of T and S to corresponding climatological values was introduced. First, it is known that the Mellor-Yamada 2.5 turbulence scheme with monthly climatological winds results in underestimating of mixing in the upper boundary layer, see, e.g., Martin (1985), Ezer (2000). Second, it is known also that to reach an established temperature and salinity distribution in the deep ocean models must be integrated for 1000 years (Bryan, 1984). But we know that both temperature and salinity tend to climatological values, so weak nudging is introduced to accelerate the process of establishment (which is common practice in many general circulation models, see, e.g., Sarmiento and Bryan, 1982; Oey and Chen, 1992). Figure A.2 shows profiles of temperature and salinity to the south of Mindanao (NPW), and to the north of the Halmahera Sea (SPW) in August after 15 years of the model run for different nudging coefficients. Near surface values of nudging coefficients for T and S for the four experiments are shown in the legend. Nudging coefficients decrease linearly from near surface values to 10^{-8} s^{-1} at 300 m for T and at 500 m for S and are constant below these depths. Based on the results shown in Figure A.2 we chose nudging coefficients in the upper layer as 10^{-5} s^{-1} both for T and S. Estimates of separate terms in the temperature and salinity equations integrated over some boxes showed that advection terms are the leading factors. The resultant advection is usually smaller. Nudging is not negligible because it played a helpful role in shaping temperature and salinity profiles, but it never played a dominant role in the corresponding equations.

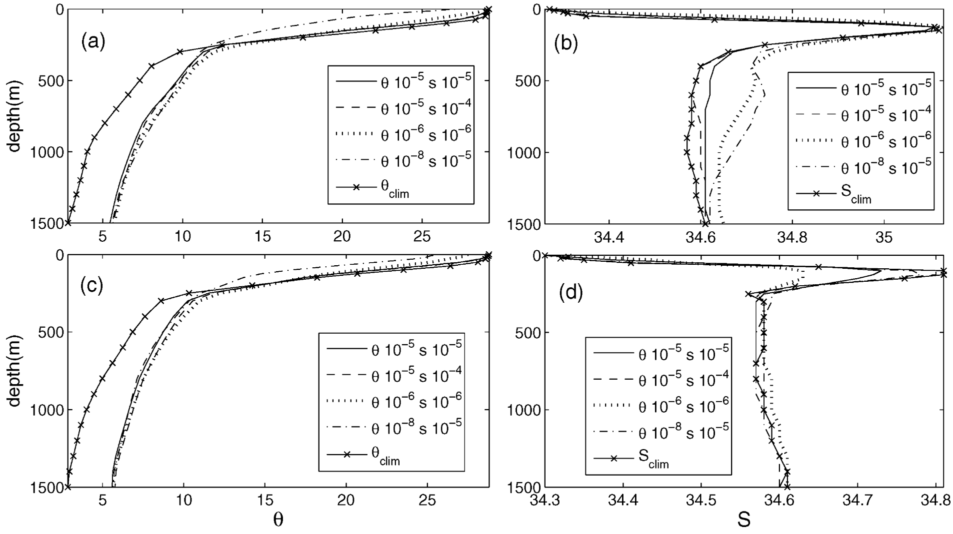

Figure A.2. Profiles of potential temperature, θ, and salinity, S, in the upper ocean for different coefficients of nudging in August to the north of the Halmahera Sea, (a) and (b), respectively, and to the south of Mindanao, (c) and (d), respectively. $\theta 10^{-5}$ s 10^{-5} implies nudging coefficient in the upper ocean for θ and S equal to 10^{-5}.

Monthly climatological winds are taken from the Comprehensive Ocean-Atmosphere Data Set (COADS), analyzed by da Silva *et al.* (1994) and are calculated at every internal time step.

v. *The boundary conditions at the solid boundaries.* We use POM recommended BCs at the solid boundaries.

c. Further modifications of the POM equations

In addition to nudging in the T, S-equations, port channels have been introduced to allow for tapering off of any possible effects of nudging at the open boundary. Therefore the basic equations have been modified within the port channels. Furthermore, to control the partition of flow in some important regions we incorporated additional frictional terms of the form $-r^{(v)}(x, y)u$, $-r^{(v)}(x, y)v$ into the momentum equations, with $r^{(v)}(x, y)$ nonzero in the vicinity of some passages and sills. The details are given in O'Driscoll (2007). This additional friction is a proxy for important tidal friction that occurs within narrow passages and at sills. The approach is rather crude but tides somehow need to be taken into account. Otherwise, due to western intensification, we obtained overly strong flows through, for example, the Lombok and Ombai Straits. A similar approach was taken by Schiller *et al.* (1998). The direct incorporation of tides is a separate difficult problem. Note that the coefficient of this additional friction was kept the same for all experiments including experiments with prescribed surface temperature and salinity.

d. Calculation of the external characteristics at internal time steps

Any external characteristics (wind, climatological T and S, etc. were represented by Fourier polynomials. First, the Fourier coefficients $A_0 \dots A_6$ and $B_1 \dots B_6$ are calculated from monthly data at every grid point. In cases when we have seasonal data only the number of Fourier coefficients was reduced. Then the Fourier components are calculated and summed up at every internal time step (10 min) and at every grid point. Transports Q_{MC}, Q_{NECC} and Q_{NGCC} were taken from observations (positive if directed out of the domain and negative otherwise). See Table A.1. The choice of these transports influences the calculated transports through basic passages, but does not determine them.

Table A.1. The prescribed transports at the open ports in Sverdrups for the Mindanao Current (MC), New Guinea Coastal Current (NGCC), North Equatorial CounterCurrent (NECC), and the Indian Ocean (IO).

	Feb 1	May 1	Aug 1	Nov 1
Q_{MC}	−25	−30	−35	−30
Q_{NGCC}	−17	−22.5	−28	−22.5
Q_{NECC}	34	40	46	40
Q_{IO}	8	12.5	17	12.5

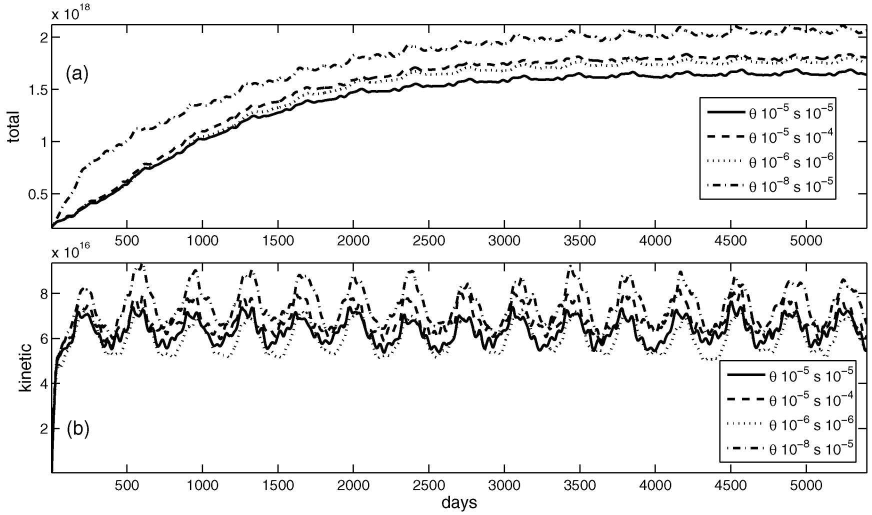

Figure A.3. Time evolution of "*total*" energy (a) and "*kinetic*" energy (b) in the upper ocean (500 m): for different nudging coefficients of θ and S in the upper layer (see Eqs. (A.8) and (A.9)).

e. Period of integration

To monitor the evolution of experiments two characteristics E_t and E_k appeared useful,

$$E_t = \int_V \left(\rho_m \frac{u^2 + v^2 + w_{pom}^2}{2} + \frac{g^2 \rho_0^2}{2\rho_m N^2} \rho'^2 \right) dV + \int_S \frac{g\rho_m}{2} \eta^2 dS, \tag{A.8}$$

$$E_k = \int_V \left(\rho_m \frac{u^2 + v^2 + w_{pom}^2}{2} \right) dV \tag{A.9}$$

where E_t is considered as the "total" energy; E_k is the "kinetic" energy; V is the domain volume; S is the horizontal area of the domain; ρ_m is the mean density determined by averaging the annual climatological density over the horizontal; N is the buoyancy frequency calculated from ρ_m; $\rho' = (\rho - \rho_m)/\rho_0$; w_{pom} is the POM vertical velocity; g is gravity. Note that E_t is equal to the total energy (kinetic plus potential), if deviations of all characteristics from corresponding climatic values are small. But E_t and E_k are always positive and we found it convenient to monitor the establishment of the model by following the variation of these characteristics (Fig. A.3).

REFERENCES

Bryan, K. 1984. Accelerating the convergence to equilibrium of ocean-climate models. J. Phys. Oceanogr., *14*, 666–673.

Burnett, W. H., V. M. Kamenkovich, A. L. Gordon and G. L. Mellor. 2003. The Pacific/Indian Ocean pressure difference and its influence on the Indonesian seas circulation: Part I - The study with specified total transports. J. Mar. Res., *61*, 577–611.

Conkright, M. E., R. A. Locarnini, H. E. Garcia, T. D. O'Brien, T. P. Boyer, C. Stephens and J. I. Antonov. 2002. World Ocean Atlas 2001: Objective Analyses, Data Statistics, and Figures, CD-ROM Documentation. National Oceanographic Data Center, Silver Spring, MD, 17 pp.

Cresswell, G. R. and J. L. Luick. 2001. Current measurements in the Halmahera Sea. J. Geophys. Res., *106*, 13945–13951.

da Silva, A. M., C. C. Young, and S. Levitus. 1994. Atlas of Surface Marine Data 1994, Volume 2: Anomalies of Directly Observed Quantities. NOAA Atlas NESDIS 7, U.S. Department of Commerce, NOAA, NESDIS.

Ezer, T. 2000. On the seasonal mixed layer simulated by a basin-scale ocean model and the Mellor-Yamada turbulence scheme. J. Geophys. Res., *105*, 16,843–16,855.

Ffield, A. and A. L. Gordon. 1996. Tidal mixing signatures in the Indonesian Seas. J. Phys. Oceanogr., *26*, 1924–1937.

Fieux, M., C. Andrie, P. Delecluse, A. G. Ilahude, A. Kartavtseff, F. Mantisi, R. Molcard and J. C. Swallow. 1994. Measurements within the Pacific-Indian oceans throughflow region. Deep-Sea Res. I, *41*, 1091–1130.

Firing, E., S. Wijffels and P. Hacker. 1998. Equatorial subthermocline currents across the Pacific. J. Geophys. Res., *103*, 21,413–21,423.

Godfrey, J. S., A. C. Hirst, and J. Wilkin. 1993. Why does the Indonesian Throughflow appear to originate from the North Pacific? J. Phys. Oceanogr., *23*, 1087–1098.

Godfrey, J. S. and J. L. Wilkin. 1995. Reply. J. Phys. Oceanogr., *25*, 1568–1570.

Gordon, A. L. 1995. When is "appearance" reality? A comment on why does the Indonesian Throughflow appear to originate from the North Pacific. J. Phys. Oceanogr., *25*, 1560–1567.

—— 2005. Oceanography of the Indonesian seas and their throughflow. Oceanography, *18*, 14–27.

Gordon, A. L. and R. A. Fine. 1996. Pathways of water between the Pacific and Indian oceans in the Indonesian seas. Nature, *379*, 146–149.

Gordon, A. L., A. Ffield and A. G. Ilahude. 1994. Thermocline of the Flores and Banda seas. J. Geophys. Res., *99*, 18235–18242.

Gordon, A. L., C. F. Giulivi and A. G. Ilahude. 2003. Deep topographic barriers within the Indonesian seas. Deep-Sea Res. II, *50*, 2205–2228.

Grist, J. P. and S. A. Josey. 2003. Inverse analysis adjustment of the SOC air-sea flux climatology using ocean heat transport constraints, J. Climate, *20*, 3274–3295.

Haney, R. 1991. On the pressure gradient force over steep topography in sigma-coordinate ocean models. J. Phys. Oceanogr., *21*, 610–619.

Hautala, S. L., J. L. Reid and N. Bray. 1996. The distribution and mixing of Pacific water masses in the Indonesian seas. J. Geophys. Res., *101*, 12375–12390.

Ilahude, A. G. and A. L. Gordon. 1996. Thermocline stratification within the Indonesian seas. J. Geophys. Res., *101*, 12401–12409.

Il'in, A. M., V. M. Kamenkovich, S. F. Kanaev, T. G. Zhugrina, and L. I. Lavrishcheva. 1974. An experiment in constructing a smoothed bottom relief of the World Ocean. Oceanology, *14*, 617–622 (Translated from Russian).

Kamenkovich, V. M., K. T. A. O'Driscoll and D. A. Nechaev. 2009. Dynamics of the Indonesian seas circulation. Part II - The role of pressure head. J. Mar. Res., *67*, 159–184.

Koch-Larrouy, A., G. Madec, B. Blanke and R. Molcard. 2008. Water mass transformation along the Indonesian throughflow in an OGCM. Ocean Dyns., *58*, 289–309.

Marchesiello, P., J. M. McWilliams, and A. Shchepetkin. 2001. Open boundary conditions for long-term integration of regional oceanic models. Ocean Model., *3*, 1–20.

Martin, P. J. 1985. Simulation of the mixed layer at OWS November and Papa with several models. J. Geophys. Res., *90*, 903–916.

Mellor, G. L., T. Ezer, and L.-Y. Oey. 1994. The pressure gradient conundrum of sigma coordinate ocean models. J. Atmos. Ocean Tech., *11*, 1126–1134.

O'Driscoll, K. T. A., 2007. A regional model of the Indonesian seas circulation. PhD Dissertation, Department of Marine Science, The University of Southern Mississippi, 169 pp.

Oey, L.-Y. and P. Chen. 1992. A model simulation of circulation in the northeast Atlantic shelves and seas. J. Geophys. Res., *97*, 20,087–20,115.

Orlanski, I. 1976. A simple boundary condition for unbounded hyperbolic flows. J. Comp. Phys., *21*, 251–269.

Sarmiento, J. L. and K. Bryan. 1982. An ocean transport model for the North Atlantic. J. Geophys. Res., *87*, 394–408.

Schiller, A., J. S. Godfrey, P. C. McIntosh, G. Meyers, and S. E. Wijffels. 1998. Seasonal near-surface dynamics and thermodynamics of the Indian Ocean and Indonesian throughflow in a global ocean general circulation model. J. Phys. Oceanogr., *28*, 2288–2312.

Sprintall, J., A. Gordon, R. Molcard, G. Ilahude, N. Bray, T. Chereskin, G. Cresswell, M. Feng, A. Ffield, M. Fieux, S. Hautala, J. Luick, G. Meyers, J. Potemra, D. Susanto, and S. Wijffels. 2000. The Indonesian Throughflow: Past, Present and Future Monitoring. Proceedings from the Sustained Observations for Climate of the Indian Ocean Workshop, Perth, Australia, November 2000, IOC/CLIVAR Technical Report.

Top, Z., A. Gordon, P. Jean-Baptiste, M. Fieux, A. G. Ilahude, and M. Muchtar. 1997. ^{3}He in Indonesian seas: Inferences on deep pathways. Geophys. Res. Letts., *24*, 547–550.

Tozuka, T., T. Qu, Y. Masumoto, and T. Yamagata. 2009. Impacts of the South China Sea Throughflow on seasonal and interannual variations of the Indonesian Throughflow. Dyns. Atmos. Oceans, *47*, 73–85.

Tozuka, T., T. Qu and T. Yamagata. 2007. Dramatic impact of the South China Sea on the Indonesian Throughflow. Geophys. Res. Letts., *34*, doi:10.1029/2007GL030420, L12612.

Van Aken, H. M., J. Punjanan, and S. Saimima. 1988. Physical aspects of the flushing of the East Indonesian basins. Neth. J. Sea Res., *22*, 315–339.

Van Riel, P. M. 1943. The bottom water, introductory remarks and oxygen content. -Snellius Exped. 1929-1930, *II*, Part 5, Chapter I. E.J. Brill, Leiden: 1–62.

Wyrtki, K., 1961. Physical oceanography of the southeast Asian waters. Univ. Calif., NAGA Rept., No. 2, 195 pp.

Received: *8 December, 2006*; revised: *29 May, 2009*.